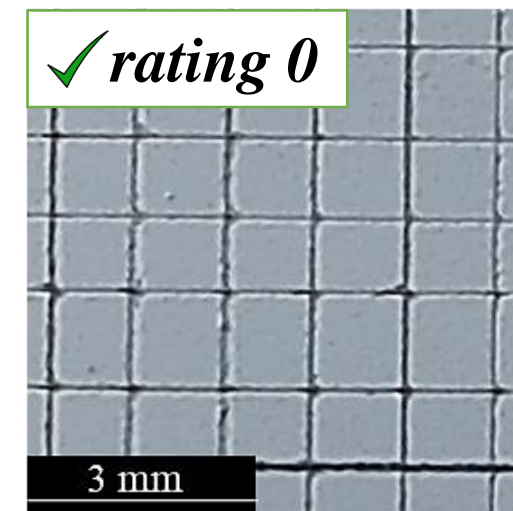
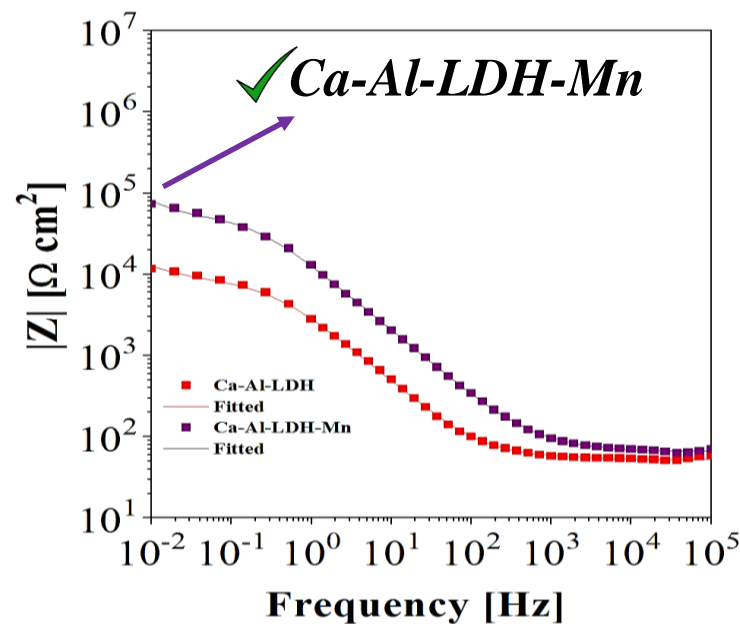
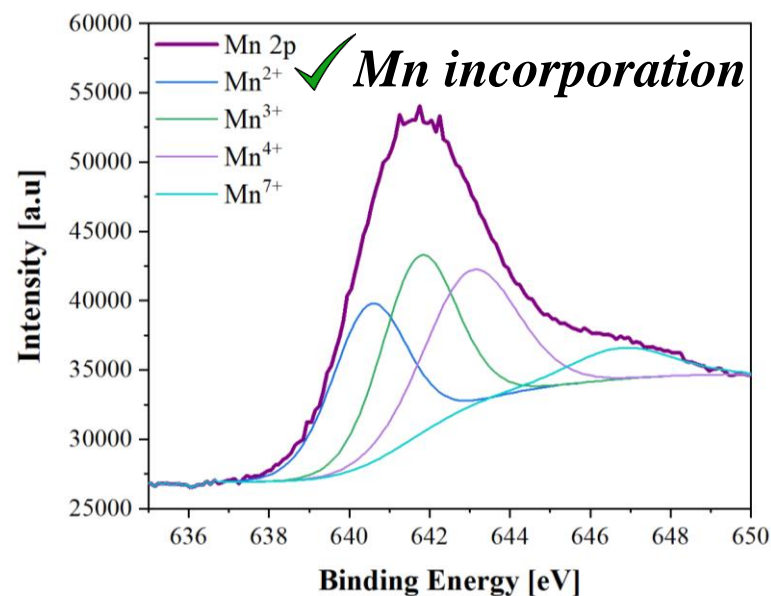


Highlights:

- The development of Ca-Al-LDH by *in situ* growth methodology on 2024-T3 alloy is studied.
- MnO_4^- species were successfully incorporated into the Ca-Al-LDH film.
- Optimum corrosion resistance and paint adhesion are achieved with Mn-doped Ca-Al-LDH coating.
- The Mn-doped Ca-Al-LDH coating provides active corrosion protection.

I) Characterization, Corrosion behaviour and Paint adhesion



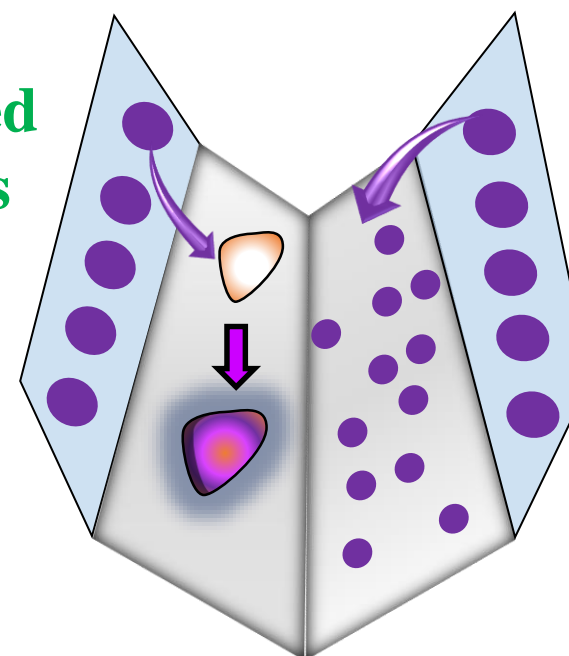
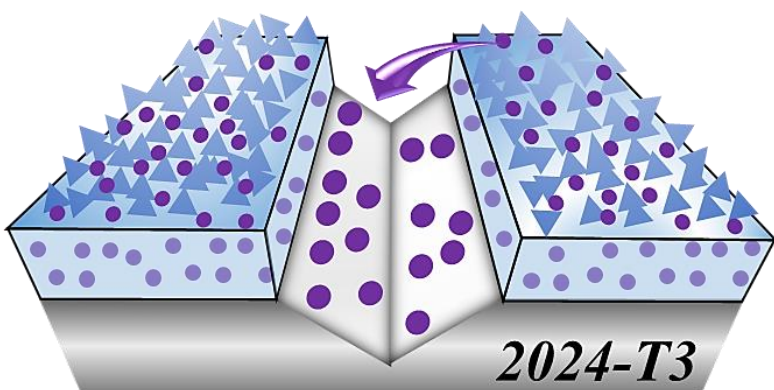
II) Active corrosion protection

Mn^{x+} Release

a) IMCs coated with Mn oxides

b) Mn-rich protective layer

Mixed inhibition



Declaration of competing interest

The authors declare that they have no known competing financial interests or personal relationships that could have appeared to influence the work reported in this paper.

Permanganate loaded Ca-Al-LDH coating for active corrosion protection of 2024-T3 alloy

Ruben del Olmo: Conceptualization, Methodology, Investigation, Experimental part, Writing- Original draft preparation. **Marta Mohedano:** Experimental part, Review & Editing, Resources, and Project Administration. **Endzhe Matykina:** Experimental part, Supervision, Review & Editing, Resources, and Project Administration. **Raúl Arrabal Durán:** Experimental part, Investigation, Supervision, Review & Editing, Resources, and Project Administration.



Click here to access/download
Supplementary Material
Supplementary material.docx



Permanganate loaded Ca-Al-LDH coating for active corrosion protection of 2024-T3 alloy

R. del Olmo^{1,2*}, M. Mohedano¹, E. Matykina¹, R. Arrabal¹

¹ *Departamento de Ingeniería Química y de Materiales, Facultad de Ciencias Químicas, Universidad Complutense, 28040, Madrid, Spain*

² *Institute of Optoelectronics, Military University of Technology, 2 Kaliskiego Str., 00-908 Warsaw, Poland*

*Corresponding author. E-mail: rubandom@ucm.es

Highlights:

- The development of Ca-Al-LDH by *in situ* growth methodology on 2024-T3 alloy is studied.
- MnO_4^- species were successfully incorporated into the Ca-Al-LDH film.
- Optimum corrosion resistance and paint adhesion are achieved with Mn-doped Ca-Al-LDH coating.
- The Mn-doped Ca-Al-LDH coating provides active corrosion protection.

Abstract: Ca-Al-Layered Double Hydroxide (Ca-Al-LDH) coating was explored on 2024-T3 aluminium alloy by *in situ* growth methodology following a 1 hour treatment at atmospheric pressure. Mn-based species were successfully incorporated into the Ca-Al-LDH structure by a low-temperature post-treatment (Ca-Al-LDH-Mn). Both LDH coatings disclosed a flaky-like morphology and low thickness ($\sim 0.6 \mu\text{m}$). Ca-Al-LDH-Mn coating showed optimal paint adhesion and the highest long-term corrosion resistance in 3.5 wt. % NaCl solution. Evaluation of scribed LDH specimens by SEM/EDS techniques up to 7 days of immersion in 3.5 wt. % NaCl solution revealed that the presence of Mn species in the Ca-Al-LDH-Mn provided active corrosion protection.

Keywords: 2024-T3; Aluminium; Layered double hydroxides; LDH; Corrosion inhibitors; Active corrosion protection.

1. Introduction

Chemical Conversion (CC) treatments aim to form a thin oxide layer on a metallic substrate by means of a chemical reaction with a suitable solution [1]. CC coatings are widely used for corrosion-sensitive applications in the aircraft industry due to their easy operation and cost-effectiveness compared to conventional anodizing. For Al alloys, chromate-based conversion coatings (CCCs) have a proven track record of over 100 years owing to their optimal paint adhesion and corrosion performance [2, 3]. However, given the intrinsic health and safety issues coming along with CCCs, chromates must be withdrawn from use and substituted by eco-friendly alternatives [4]. Cr-free alternatives have been an ongoing research topic for more than 20 years [5, 6]. A wide range of treatments based on Mn-, Ce-, Mo-, Li- and V-species have been investigated, demonstrating the array of alternative chemistries available for aluminium [3, 7-9]. Nevertheless, these processes often struggle to fulfil the stringent requirements of the aircraft industry.

More recently, there has been an increasing interest in the development of layered double hydroxides (LDHs) [10-12]. LDHs can be described as positively charged mixed metal [M(II)-M(III)] hydroxide layers and interlayers occupied by anions and water molecules. The general formula of LDHs can be represented as $[M^{II}_{1-x}M^{III}_x(OH)_2]^{x+}[(A^{m-})_{x/n} \cdot nH_2O]^{x-}$, where M(II) and M(III) represent divalent (e.g., Mg^{2+} , Ca^{2+} , Cu^{2+} , Zn^{2+}) and trivalent metallic cations (e.g., Al^{3+} , Fe^{3+} , Co^{3+}), respectively, and A^{m-} represents the interlayer anion (e.g., Cl^- , CO_3^{2-} , NO_3^-). LDH properties can be tailored by controlling the size, charge, and ratio of the metal cations and anions. These parameters also determine the crystal structure and the anion-exchange capacity [10, 11]. LDH synthesis methods can be costly and time consuming [11, 13, 14]. However, the *in situ* method is cost-effective, versatile, and relatively simple, therefore, suitable for mass-production. For instance, a ~2 μm -thick coating can be produced by immersing Al (source of Al^{3+}) into a M^{2+} -containing solution at specific pH conditions [15, 16].

The anticorrosion properties of LDH coatings are attributed to their barrier effect and anion-exchange capacity. Furthermore, active corrosion protection can be implemented by means of inhibitor loading [17]. The active protection mechanism is triggered at the location of coating defects by changes in pH or other factors, resulting in the release of corrosion inhibitors and entrapment of corrosive anions (e.g., Cl^-) within the interlayer

galleries. This mechanism, in principle, should ensure long-term corrosion protection [15, 18].

In the case of 2024-T3 alloy, corrosion studies have been focusing on di- (Zn^{2+} , Mg^{2+}) and trivalent (Ce^{3+}) Al-LDH coatings formed by the *in situ* approach (Table 1). On average, LDH coatings increase the corrosion resistance by one order of magnitude (measured by potentiodynamic polarization, PDP, and impedance modulus at low frequencies, $|Z|_{10\text{mHz}}$) in comparison to the bare alloy.

Table 1. Examples of corrosion studies on inhibitor-loaded LDH coatings grown on AA2024-T3 by the *in situ* method.

LDH Recipe/conditions	Post-treatment/Thickness	Corrosion	Ref
Mg/Al-LDH 0.038 M MgSO_4 0.075 M $\text{Al}_2(\text{SO}_4)_3$ 0.595 M H_2NCONH_2 (90-120) °C; 9h.	- Vanadate-loading: 24 h in 0.38 M Vanadate solution (No T data, pH: 4.5-5.5). - Sol-Gel coating - Thickness: LDH-V/Sol-gel: 5.8 μm .	$ Z _{10\text{mHz}}$ ($\Omega \cdot \text{cm}^2$) in 3.5 wt. % NaCl - LDH/Sol-gel: 10^4 (0.5 h) and $4 \cdot 10^4$ (24-480) h - LDH-V/Sol-gel: $\sim 10^5$ (0.5-480) h	[19]
Zn/Al-LDH $\text{Zn}(\text{NO}_3)_2$ solution pH: neutral range < 100 °C; Few hours.	- Vanadate-loading: Immersion in NaVO_3 solution (no concentration data) (< 50 °C and pH: 8-9). - Thickness: LDH-V: 3-7 μm	$ Z _{10\text{mHz}}$ ($\Omega \cdot \text{cm}^2$) in 2.9 wt. % NaCl Unsealed: $4 \cdot 10^3$ (25 min); 10^4 (720h) LDH: $1 \cdot 10^6$ (25 min); 10^5 (720h) LDH-V: $3 \cdot 10^5$ (25 min); $2 \cdot 10^5$ (720h)	[18]
Zn/Al-LDH 0.005 M $\text{Zn}(\text{NO}_3)_2$ pH: neutral range < 100 °C; 168-300 h.	- Vanadate-loading: Immersion in NaVO_3 solution (no concentration data) (< 50 °C and pH: 8-9). For a few hours. - Thickness: No data	$ Z _{10\text{mHz}}$ ($\Omega \cdot \text{cm}^2$) in 2.9 wt. % NaCl Zn-Al-LDH: 10^5 (168 h); 10^3 (350 h) Zn-Al-LDH-V: $7 \cdot 10^5$ (700 h)	[20]
Zn/Al-LDH 0.05 M $\text{Zn}(\text{NO}_3)_2$ 0.3 M NH_4NO_3 45 °C, 6 h; pH: neutral.	1- Vanadate-loading: Immersion in 0.1 M NaVO_3 (pH: 8.8 ± 0.2). 2- Molybdate-loading: Immersion in 0.1 M Na_2MoO_4 (pH: 8.8 ± 0.2). 3- MBT-loading: Immersion in 0.1 M NaMBT solution (pH:10). All reactions were performed at 45°C and 2 h. -Thickness: No data	PDP (E_{corr} (V); i_{corr} ($\text{A} \cdot \text{cm}^{-2}$)) in 2.9 wt. % NaCl Unsealed: -0.55; $1.04 \cdot 10^{-5}$ Zn-Al-LDH: -0.51; $4.2 \cdot 10^{-6}$ Zn-Al-LDH-V: -0.46; $9.44 \cdot 10^{-8}$ Zn-Al-LDH-Mo: -0.50; $5.25 \cdot 10^{-7}$ Zn-Al-LDH-MBT: -0.45; $5.57 \cdot 10^{-7}$	[21]

Zn/Al/Ce-LDH: 0.05 M Zn(NO ₃) ₂ 0.005 M Ce(NO ₃) ₃ 0.3 M NH ₄ NO ₃ - 70 °C; 24 h.	-Vanadate-loading: Immersion in 0.1 M NaVO ₃ solution (45 °C and pH: 8.8 ± 0.2). For 2 hours. - Thickness: ZnAlCe/V ₂ O ₇ : 2 µm	Z _{10 mHz} (Ω·cm ²) in 2.9 wt. % NaCl ZnAl-NO ₃ : 4·10 ³ (24 h), ZnAlCe-NO ₃ : 10 ⁴ (24 h) ZnAlCe/ V ₂ O ₇ : 10 ⁶ (24 h); 2·10 ⁶ (336 h) [22]
Zn/Al-LDH: 0.05 M Zn(NO ₃) ₂ 0.3 M NH ₄ NO ₃ - 45 °C, 6 h; pH: neutral.	- Molybdate-loading: Immersion in 0.1 M Na ₂ MoO ₄ (45 °C and pH: 10). For 2 hours. - Thickness: 1. LDH-MoO ₄ : 15.605 nm 2. LDH-MoO ₄ /GN: 12.217 nm	Z _{10 mHz} (Ω·cm ²) in 3.5 wt. % NaCl LDH-MoO ₄ : 4·10 ⁴ MoO ₄ /GN: 2·10 ⁵ [23]

It is important to note that most of the examples shown in **Table 1** are concerned with LDH coatings that are thicker than CCCs (0.05-2 µm). This poses a major challenge for fatigue-critical components in the aircraft industry [4]. Besides, long treatment times and high temperatures (> 6h; >100 °C) are often used, thereby limiting commercial acceptance of LDH.

Regarding the use of corrosion inhibitors on LDH-coated 2024-T3 alloy, vanadate (VO₄³⁻) and permanganate (MoO₄²⁻) anions have been successfully intercalated into Zn-Al-LDH (**Table 1**). MoO₄²⁻ ion is known to behave as an anodic inhibitor, whereas VO₄³⁻ ion is considered to be a mixed inhibitor for aluminium, suppressing both anodic and cathodic reactions. In this scenario, Zn-Al-LDHs loaded with VO₄³⁻ can be considered promising candidates for substituting CCCs. However, VO₄³⁻ ions have been categorised as equally toxic as chromate [24]. Therefore, the search for Cr- and V-free alternatives is still an important research topic.

Ca-Al-NO₃ represents an alternative to the Zn-Al system as it stands out for its excellent exchange ability with several anionic species (e.g., CO₃²⁻, PO₄³⁻ and long fatty acids) [25-27]. For instance, Ahsan Iqbal *et al.* [28] produced a Ca-Al-LDH coating by *in situ* growth methodology on 6082 alloy and reported an increase in the |Z|_{10mHz} by almost three orders of magnitude compared to the bare alloy.

Up to date, there are no available data on the *in situ* growth of Ca-Al-LDH on 2024-T3 alloy, which is the most widely used Al alloy in the aircraft industry. In addition, other aspects remain unclear. For instance, there is no available data on the paint adhesion for inhibitor-containing LDH systems, which is a key parameter for the aircraft industry, as CCCs would typically constitute a part of a multi-layer coating system. In the present study,

different aspects are investigated with the aim to fill up some of these knowledge gaps:
 (i) *in situ* growth of a Ca-Al-LDH coating on 2024-T3 using short treatment times at atmospheric pressure; (ii) incorporation of MnO_4^- as eco-friendly corrosion inhibitor into the LDH structure; and (iii) evaluation of active corrosion protection and paintability.

2. Experimental part

2.1. Specimen preparation

The base aluminium alloy used for this study is AA2024-T3 (wt. %: 3.8-4.9 Cu, 1.2-1.8 Mg, 0.3-0.9 Mn, <0.5 Fe, <0.5 Si, <0.25 Zn, <0.15 Ti, <0.1 Cr and Al balance) supplied by *SMW Engineering Group*.

The samples were cut from sheets into rectangular specimens ($20 \times 25 \times 1.5 \text{ mm}^3$) and pre-treated following an industrial procedure recommended by *Henkel*. The 2024-T3 specimens were immersed in 70 g L^{-1} BONDERITE C-AK 4215NC solution for 10 min at 60°C and etched in 85 g L^{-1} BONDERITE C-AK ALUM ETCH 2 AERO at 40°C for 2 min. Each procedure was followed by rinsing in deionized water. Finally, specimens were desmutted by immersion in BONDERITE C-IC SMUTGO NC AERO for 5 min, rinsed in deionized water and, dried with warm air.

2.2. LDH synthesis

The synthesis of Ca-Al-LDH and Ca-Al-LDH-Mn was carried out at $\sim 95^\circ\text{C}$ for 1 hour following the steps depicted in **Figure 1**. Specimens were vertically immersed in a $0.1 \text{ M Ca(NO}_3)_2 \cdot 4\text{H}_2\text{O}$ and $0.3 \text{ M NH}_4\text{NO}_3$ aqueous solution at pH ~ 10 . The pH value was adjusted by adding 2M NaOH solution. After rinsing in deionized water and drying with warm air, the specimens were post-treated by immersion in a 0.1 M KMnO_4 solution at $\sim 45^\circ\text{C}$ for 2 h (pH ~ 10). The rinsed and dried Ca-Al-LDH and Ca-Al-LDH-Mn specimens were stored in a desiccator for at least 24 h before use.

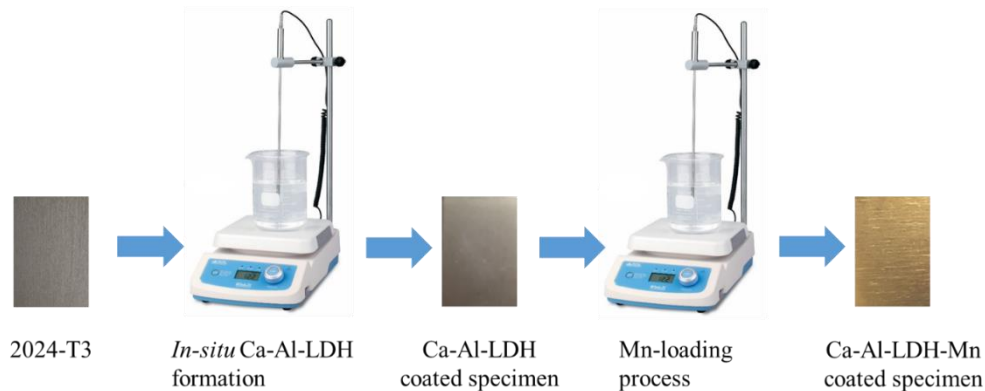


Figure 1. In-situ growth method scheme for LDH conversion coatings on the 2024-T3 alloy.

Note that this experimental procedure was selected after a screening process (**Table 1** and **Figure S1**) based on: (i) visual uniformity of the coating and (ii) the value of the impedance modulus (Z 10^{-2} Hz) obtained by electrochemical impedance spectroscopy (EIS) in 3.5 wt. % NaCl. The latter gave an estimation of the short-term corrosion resistance of the coatings studied, where higher values of $|Z|$ indicate a lower corrosion rate. In this screening, different $\text{Ca}(\text{NO}_3)_2$ concentrations (0.05-0.2 M), temperatures (70-95°C), treatment times (15-360 min) and pH values (6.5-10) were evaluated.

2.3. Characterization of LDH-coated specimens

Planar and cross-sectional views of LDH-coated specimens were examined using JEOL JSM 6335F field emission scanning electron microscope (FESEM) working at 15 kV and equipped with an energy dispersive (EDS) spectrometer for semi-quantitative analysis. For detailed analysis, cross-sectional views of LDH-coated specimens were examined by transmission electron microscopy (TEM) using a JEM 2100 instrument with an accelerating voltage of 200 kV. 20 nm-thin TEM specimens were prepared by sectioning in an ultramicrotome (Leica Ultracut S) with a diamond knife (Microstar Technologies Inc.).

The phase composition of LDH-coated specimens was carried out by XRD analysis using a Philips X'Pert-MPD instrument ($\text{Cu K}\alpha = 1.54056 \text{ \AA}$). The XRD spectra were acquired with a 0.1° grazing incidence and in the range of 2θ from 10° to 40° with a step size of 0.05° and a dwell time of 6 s per step. Phase analysis was evaluated using X'Pert High Score software and the PDF4+ database.

Real and topographic 2D and 3D images were obtained with an InfiniteFocusSL optical profilometer (ALICONA InfiniteFocusSL, GmbH). Topographic information was analysed with the IF-Measure Suite software to extract roughness parameters, such as R_a (arithmetic mean value in a roughness profile) and S_a (the difference in height of each point compared to the arithmetical mean of the surface).

Fourier transform infrared spectroscopy (FTIR) analysis was conducted with a FTIR Nicolet iS50 instrument (Thermo Fisher Scientific) equipped with a KBr beam splitter and a DTSG-KBr detector. The FTIR spectra were performed in the range of frequency from 4000 to 400 cm^{-1} . Resolution and number of scans were set to 0.5 cm^{-1} and 7500, respectively.

XPS analysis was conducted with a Fisons MT500 spectrometer (XPS) equipped with a hemispherical electron analyzer (CLAM 2) and an Mg K α X-ray source operating at 300 W, following the experimental procedure described in [29]. Spectra were acquired after 10 min Ar ion bombardment (AIB). The AIB was performed using an EXO5 ion gun incorporated into the equipment, provided with a scanning unit to track the beam, and operating at a voltage of 5 kV, an intensity of 10 mA, and 1×10^{-7} Torr of pressure. The wettability of selected specimens was evaluated with deionized water using an FTA 1000/FTA instrument and the FTA32 software. Cited values for each LDH coating are the average of 6 drops (3 in each of the two specimens).

2.4. *Electrochemical impedance spectroscopy (EIS)*

EIS was performed to evaluate the corrosion resistance of all coated specimens in an aqueous saline solution (3.5 wt. % NaCl) at room temperature. Specimens with an exposed area of 1 cm² were used in a three-electrode cell with a GillAC potentiostat (ACM Instruments). A graphite rod and silver–silver chloride (Ag/AgCl, 3 M KCl) were used as counter and reference electrodes, respectively. A sinusoidal perturbation of 10 mV amplitude in the frequency range of 30 kHz–0.01 Hz was applied after different immersion times (up to 28 days). All measurements were repeated at least twice. Equivalent circuits were simulated by using ZView software. Fits of the experimental data were obtained with chi-squared values in the range of 0.0001–0.001.

2.5. *Paint adhesion*

Dry paint adhesion test was carried out by triplicate in accordance with EN ISO 2409 standard using a 6 line cross-cut with 1 mm spacing. The rating system (from 0 to 5) is based on the detached surface area after the test, considering 0 optimal (no detachment) and 5 complete detachment. The epoxy primer 37076 used in this study was supplied by *AkzoNobel* and applied in-house with a metallic paint roller, followed by curing at 80 °C for 1 hour.

2.6. *Active corrosion protection in scribed specimens*

LDH-coated specimens, with and without inhibitor, were manually scribed with a tungsten carbide tip across the sample surface (the depth of the scribe was larger than the coating thickness and reached the underlying substrate). Hereafter, specimens were immersed in an aqueous 3.5 wt. % NaCl solution up to 7 days of exposure. Changes in the coating and the scribe were monitored using a digital stereomicroscope (BMS

Breukhoven), equipped with a 5-megapixel digital camera, and by SEM/EDS examination.

3. Results and discussion

3.1. Characterization of the coatings

Figure 2 shows the surface, optical profilometry 2D micrographs, and 3D topographical maps of the Ca-Al-LDH and Ca-Al-LDH-Mn coatings. The roughness values are presented in **Table 2**. Visible scallops or round cavities on both surfaces correspond to locations of secondary phases that were removed during the applied pre-treatment. The Mn-based post-treatment renders the surface golden. This is likely associated with MnO_4^- incorporation and formation of Mn-rich compounds which are typically brown/yellow [30]. No significant topographic changes are observed on the 2D and 3D optical profilometry micrographs. Slightly higher values of roughness are obtained in the case of the Ca-Al-LDH-Mn specimen.

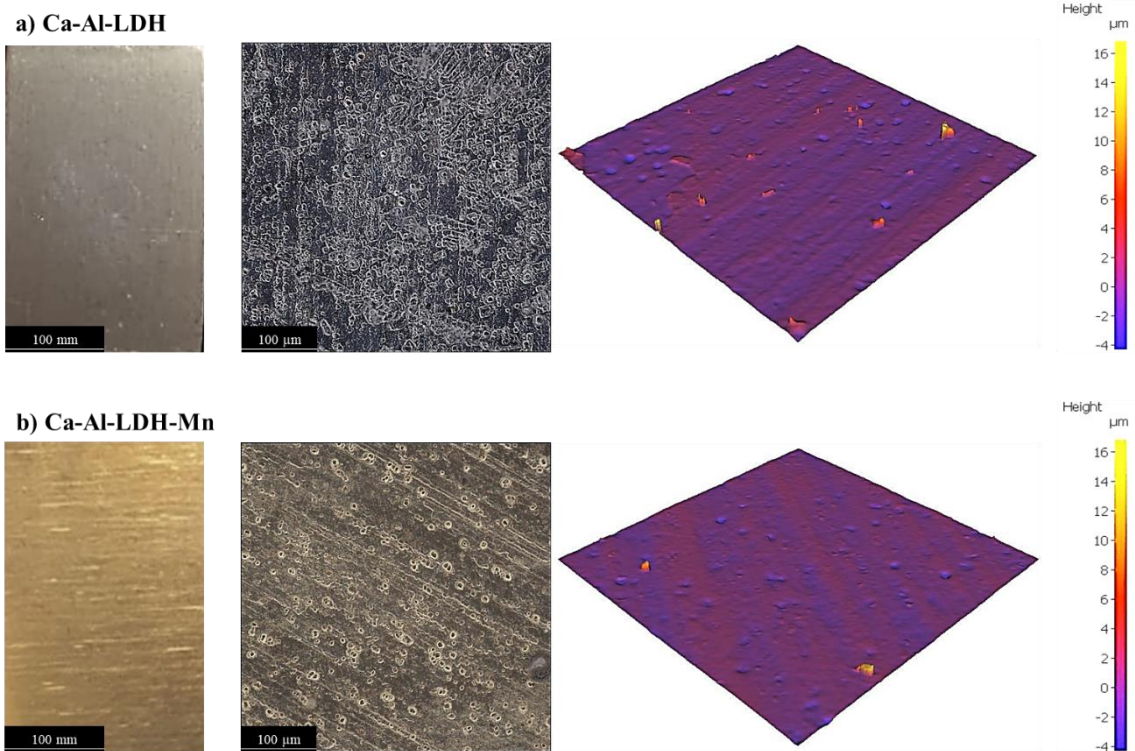


Figure 2. Surface appearance and optical profilometry micrographs of (a) Ca-Al-LDH and (b) Ca-Al-LDH-Mn coatings, including the 2D-real colour images and 3D-topographical maps.

Table 2. Roughness values of studied Ca-Al-LDH-based coatings on 2024.

Roughness (μm)	Ca-Al-LDH	Ca-Al-LDH-Mn
Ra	0.10 ± 0.01	0.30 ± 0.02
Sa	0.30 ± 0.02	0.40 ± 0.02

Scanning electron micrographs reveal that the Ca-Al-LDH and Ca-Al-LDH-Mn coatings consist of flakes that are uniformly spread across the surface (**Figure 3**).

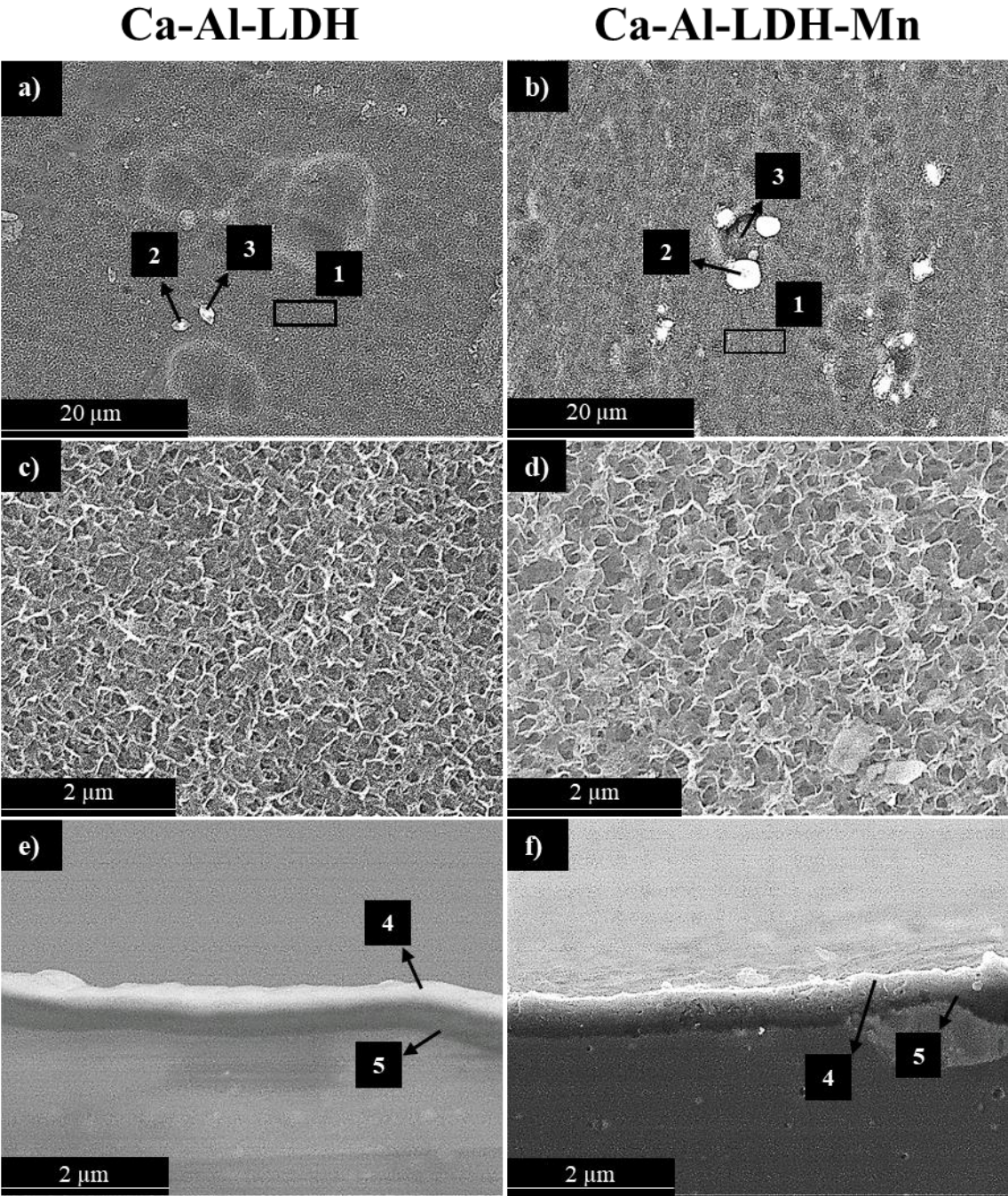


Figure 3. Planar view (a-d) and cross-sectional view (e, f) of secondary electron micrographs of Ca-Al-LDH and Ca-Al-LDH-Mn coatings on 2024 alloy.

It is important to note that flakes are relatively small due to the operating conditions used in this study (1 hour and 95 °C). Other studies, with longer treatment times (>12 h) and higher temperatures (140 °C), show larger flakes [27, 28].

Cross-sectional micrographs of Ca-Al-LDH (**Figure 3e**) and Ca-Al-LDH-Mn (**Figure 3f**) reveal a similar thickness of approximately 0.6 µm for both coatings. However, some localized thickness heterogeneity can be also observed, especially in the proximity of the intermetallic particles (**Figure 3f**). These thickness values are considerably lower in comparison to the available literature related to Ca-Al-LDH coating formed by *in situ* growth methodology [28]. This is mainly related to the low temperature and treatment times used in this study.

According to the EDS results presented in **Table 3**, the contents of Al, Cu, and Mg coming from the substrate were similar for both Ca-Al-LDH and Ca-Al-LDH-Mn coatings (areas marked as 1 in **Figure 3**).

Table 3. EDS (at. %) area analysis of Ca-Al-LDH and Ca-Al-LDH-Mn coatings on 2024 alloy.

Coating	Location		O	Al	Ca	Mn	Cu	Mg	Fe
Ca-Al-LDH	Longitudinal view	1	55.6	43.0	-	-	0.3	1.0	0.1
		2	65.2	33.4	0.1	-	0.6	0.4	0.3
		3	70.0	29.1	0.1	-	0.3	0.3	0.2
	Cross-section view	4	52.8	45.3	0.1	-	1.0	0.8	-
		5	56.2	43.0	-	-	0.2	0.6	-
Ca-Al-LDH-Mn	Longitudinal view	1	46.4	52.0	-	0.4	0.4	0.8	-
		2	84	5.5	0.5	9.2	-	0.3	0.5
		3	69.4	21.1	0.2	2.0	5.3	1.8	0.2
	Cross-section view	4	68.1	29.8	0.3	1.0	0.2	0.5	0.1
		5	24.6	64.7	-	1.0	6.5	0.2	3.0

The EDS analysis shows that Ca was only detected at low concentration (~ 0.1-0.5 at. %) and preferentially located within white round deposits (points 2 and 3 in **Figures 3a** and **3b**) and in the external outer layer (points 4 in **Figures 3e** and **3f**). The limited incorporation of Ca into the LDH structure may be related to the experimental conditions used in the present study (95 °C and 1 h). This is in line with the study of Ashan Iqbal *et al.* [28]. In that work, Ca-Al-LDH coatings were prepared at higher temperatures (140°C) and longer treatment times (12-72 h) compared to the present study. This resulted in

higher incorporation of Ca (Ca/Al wt. % ratio: from 1:7 to 1:4 for 12 and 72 h, respectively) than that found in the present study (**Table 3**).

After the inhibitor post-treatment, Mn is detected in both plan view and cross-section of the LDH coating, which is in agreement with the colour change observed in the optical images. A particularly high amount of this element along with a high amount of O is found in the white round deposits. It is important to mention that these Mn-enriched deposits are surrounding or covering intermetallic particles as deduced from the significant amount of Mg, Fe, and Cu (points 2 and 3 in **Figure 3b**).

This is probably due to the cathodic nature of secondary phases facilitating the reduction of Mn(VII), presumably to form lower valence Mn oxides/hydroxides [31-34]. Besides, it is well-known that reduction of Mn(VII) to Mn(II) is highly favoured in alkaline media (pH: ~9-12) [32, 35, 36]; in this study, the Mn-loading process was carried out at pH 10.

XRD patterns of the Ca-Al-LDH and Ca-Al-LDH-Mn coatings formed on the 2024 substrate are shown in **Figure 4**. Al peaks from the substrate are present due to the small thicknesses of LDH coatings, which are below the penetration depth of the X-rays.

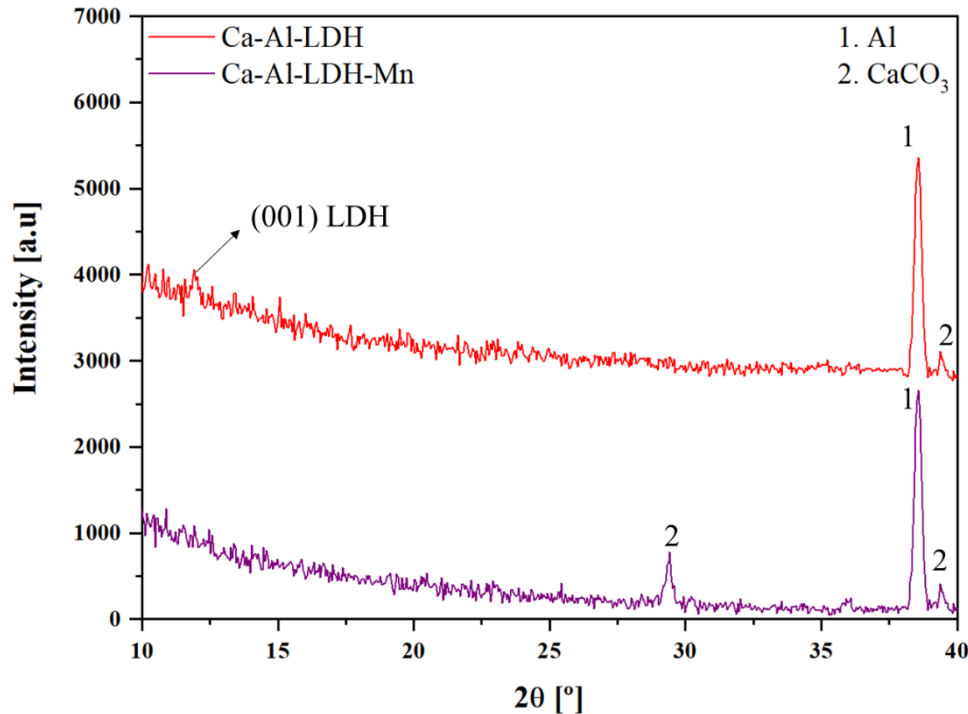


Figure 4. XRD patterns of Ca-Al-LDH and Ca-Al-LDH-Mn coatings on 2024 alloy.

A small diffraction peak at $\sim 12^\circ$ was detected for the Ca-Al-LDH specimen. This was insufficient for a sound identification, but it is located in the characteristic region of LDH phases, particularly near the (001) diffraction of Ca-Al-LDH (JCPDS #870493) [37, 38]. In the case of Ca-Al-LDH-Mn, no (001) LDH diffractions were observed. This could be associated with the presence of Mn in the Ca-Al-LDH structure that causes broadening/shifting of the diffraction peak [39, 40], making the already small (001) peak indistinguishable. However, as shown by SEM micrographs, the characteristic flakes of LDH coatings are still visible, indicating that the permanganate post-treatment did not destroy the LDH scaffold.

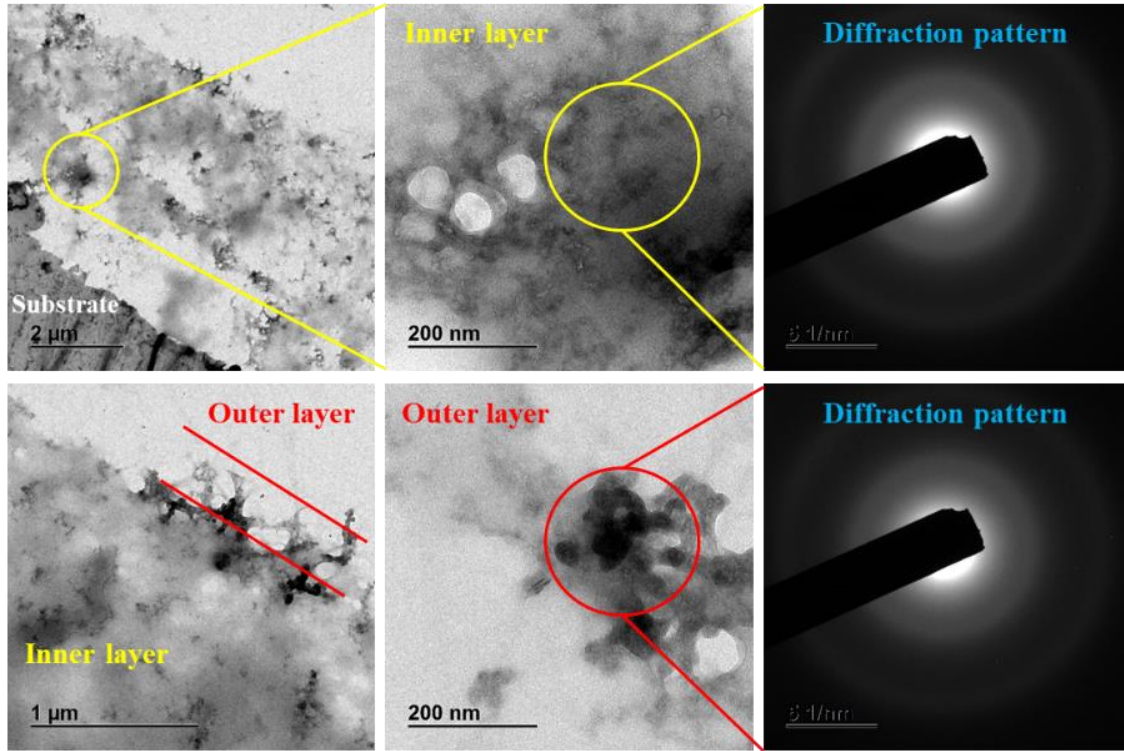
The presence of CaCO_3 (JCPDS #862334) may arise from the interaction of free aqueous Ca^{2+} with CO_3^{2-} anions coming from atmospheric CO_2 contamination during the LDH synthesis [38, 41]. An additional CaCO_3 peak was detected in the Ca-Al-LDH-Mn coating. This can be related to: (i) further interaction of Ca^{2+} with CO_3^{2-} during the Mn-loading step under atmospheric conditions, and (ii) the alkaline conditions during post-treatment (pH 10) favouring CaCO_3 precipitation [42].

Note that no additional Ca-containing phases were identified, probably due to the short treatment time used in this study (1 hour). For instance, according to Ahsan Iqbal *et al.* [28], who developed a Ca-Al-LDH coating on the 6082 alloy at treatment times between 12 and 72 h, Ca-containing phases such as $\text{Ca}(\text{OH})_2$ ($\sim 17.5^\circ$) and tricalcium aluminate ($\sim 27.5^\circ$) were detected after long treatment times.

Figure 5 depicts the cross-sectional transmission electron micrographs of Ca-Al-LDH and Ca-Al-LDH-Mn. Both coatings disclose a two-layered structure, comprising a porous inner layer and a thinner flaky layer at the top.

This double layer morphology is in agreement with recent results on a Mg-Al-LDH coating on 6082 alloy [43] and Zn-Al-LDH on 2024 alloy [44]. Note that the coatings appear to have suffered knife damage to some extent, hence the relatively loose morphology. The corresponding TEM diffraction patterns of both inner and outer parts of the Ca-Al-LDH coating reveal diffusive rings typical of a mixture of largely amorphous and some nanocrystalline material (**Figure 5a**). These diffraction patterns are in agreement with the small size of the (001) diffraction peak in the XRD pattern (**Figure 4**). As shown by the TEM micrographs (**Figure 5b**), the subsequent permanganate post-treatment did not alter the overall morphology and the amorphous/nanocrystalline nature of the LDH coating.

a) Ca-Al-LDH



b) Ca-Al-LDH-Mn

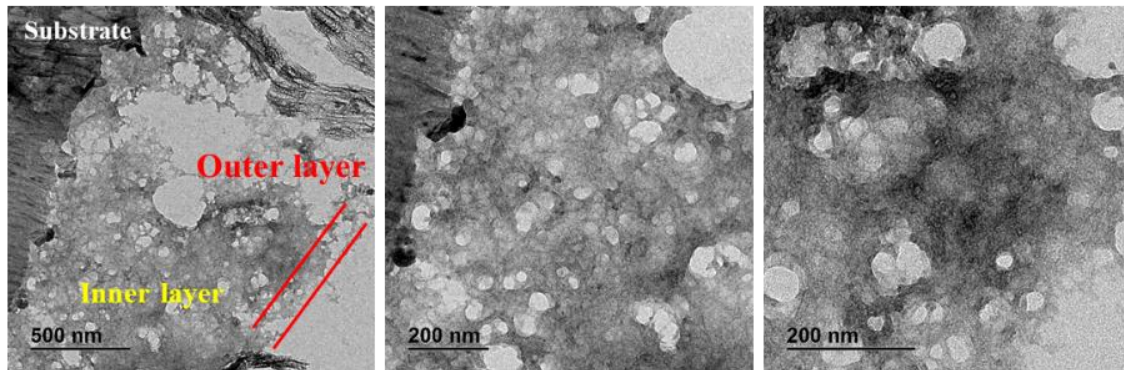


Figure 5. Transmission electron micrographs of (a) Ca-Al-LDH and (b) Ca-Al-LDH-Mn coatings on 2024-T3 alloy.

FTIR spectra of the Ca-Al-LDH and Ca-Al-LDH-Mn specimens are shown in **Figure 6**. Both studied LDH coatings showed similar absorption bands assigned to bond vibrations of the LDH layers and interlayer anions. Namely, the broad absorption band at 3400 cm^{-1} corresponds to the stretching bond vibration mode of H-OH (water molecules) and M-OH (M= Ca, Al) in the LDH structure. Note that this band is more intense for Ca-Al-LDH-Mn coating. This is associated with the formation of hydrogen bonds between water molecules and carbonate ions in the LDH interlayers [45]. The small band at $\sim 1600\text{ cm}^{-1}$ corresponds to the bending stress of the interlayer water molecules [35, 46]. Small bands

at 1380 cm^{-1} and 900 cm^{-1} correspond to the stretching vibrations of NO_3^- and CO_3^{2-} anions, respectively. The presence of these anions in the LDH interlayer balance the positive charge of the studied Ca-Al-LDH coating [17, 45].

In the low-frequency range, the band spectra at 400-800 cm^{-1} is associated with M-O, M-OH (M=Ca, Al) and CO_3^{2-} stretching bond vibrations [35, 47]. There is a clear difference between both spectra in this range since a more intense band and small shoulders can be discerned in the Ca-Al-LDH-Mn coating. This may be associated with the overlapping of additional Mn-related bond vibrations into the Ca-Al-LDH structure. Namely, small bands observed at $\sim 540 \text{ cm}^{-1}$ and 660 cm^{-1} arise from the stretching vibration of the Mn-O-Mn and Mn-O bonds, respectively [48, 49].

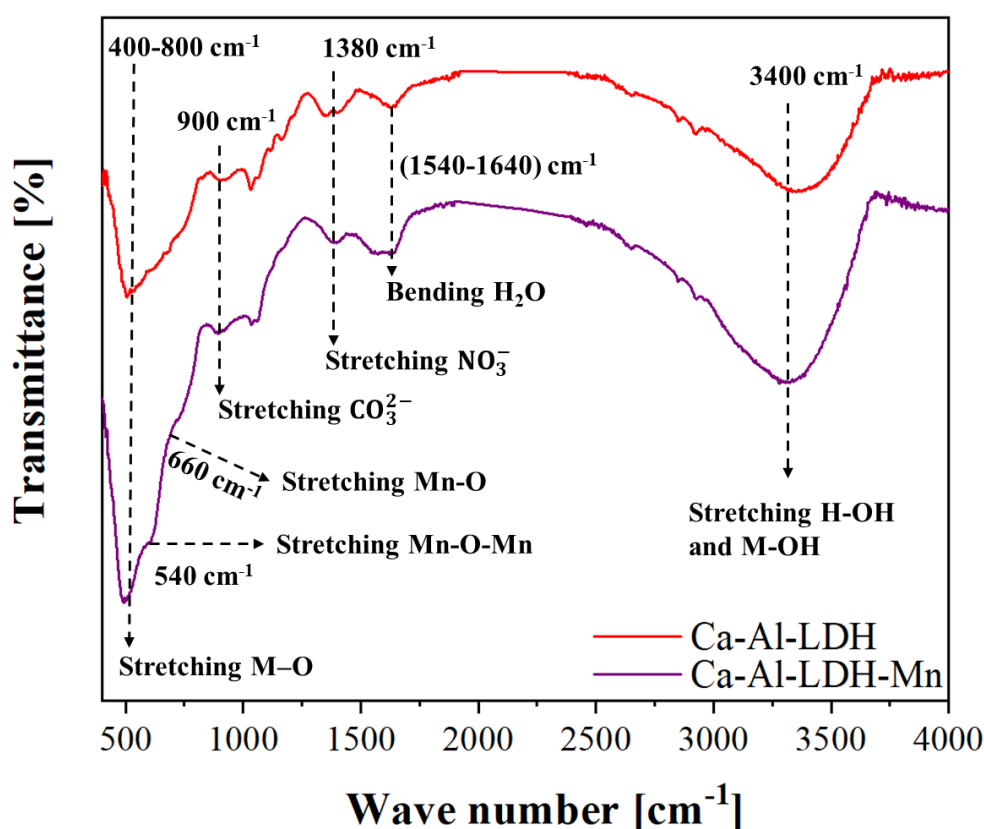
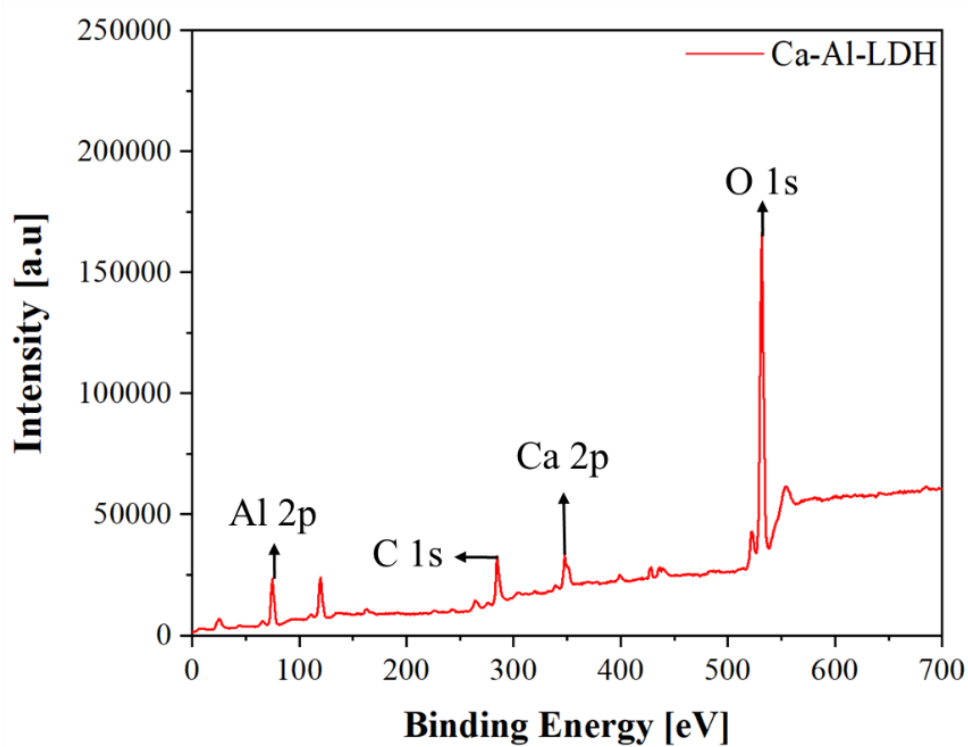


Figure 6. FTIR spectra of Ca-Al-LDH and Ca-Al-LDH-Mn coatings on 2024 alloy.

Figure 7 shows the XPS survey spectra obtained for Ca-Al-LDH and Ca-Al-LDH-Mn coatings. Both coatings show Al, C, Ca, and O peaks. Successful incorporation of Mn is also manifested at the high energy end of the spectra, along with the characteristic peak of K 2p which comes from KMnO_4 (**Figure 7b**). After peak fitting, the content of these elements was calculated (**Table 4**).

a) Ca-Al-LDH



b) Ca-Al-LDH-Mn

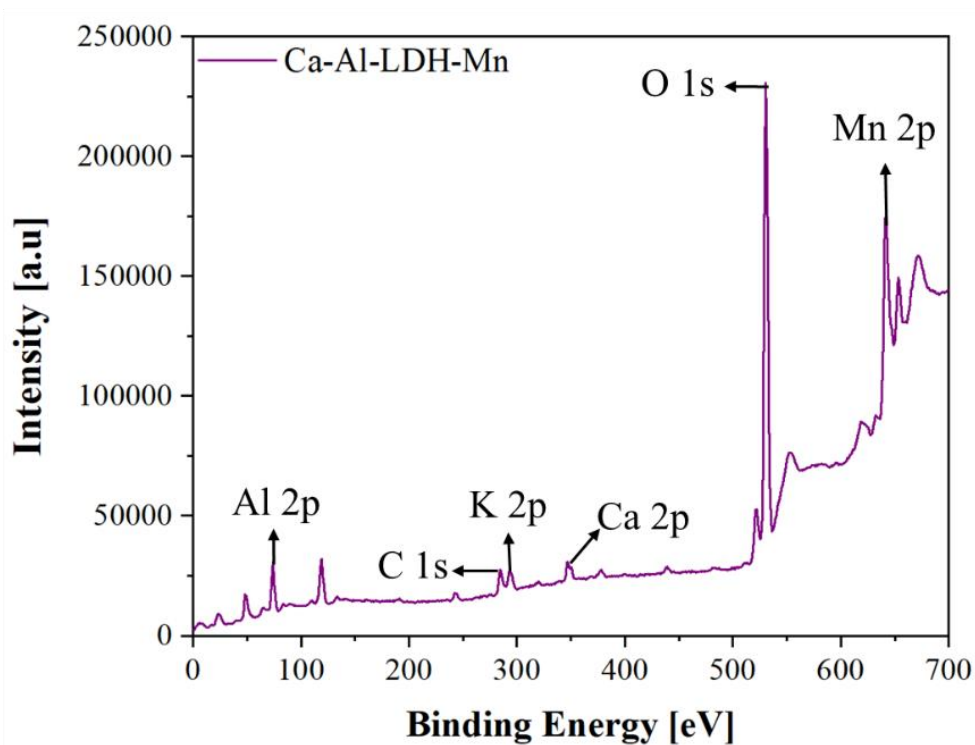


Figure 7. Survey XPS spectra of (a) Ca-Al-LDH and (b) Ca-Al-LDH-Mn coatings.

Table 4. XPS results of Ca-Al-LDH and Ca-Al-LDH-Mn coatings. Note that K was deliberately not included in the Ca-Al-LDH-Mn.

Element	Binding energy (eV)	at. %
Ca-Al-LDH		
O 1s	531.8	52.4
C 1s	287.7	20.9
Ca 2p	349.9	2.8
Al 2p	75.3	23.9
Ca-Al-LDH-Mn		
O 1s	531.0	57.0
C 1s	287.1	10.4
Ca 2p	349.1	1.3
Al 2p	74.4	19.8
Mn 2p	641.7	11.5

The high resolution Al 2p spectra show slightly different binding energies for Ca-Al-LDH (75.3 eV) and Ca-Al-LDH-Mn (74.4 eV) (**Figure S2**). Wang *et al.* [50] observed a similar shift when increasing the LDH synthesis time and associated it with the gradual conversion of Al₂O₃ (75 eV) into Al(OH)₃ (74.2 eV). In the present study, it is suggested that the Mn-loading post-treatment (45 °C, 2 h) produces an analogous effect.

The O 1s spectra (~530 to 532 eV) (**Figure S3**) of both Ca-Al-LDH and Ca-Al-LDH-Mn coatings is associated with the presence of (i) OH⁻ ions (~531.5 eV), (ii) CO₃²⁻ anions (~531.8 eV), (iii) Ca-O (~530.3 eV) and (iv) Al-O (~531.8 eV) bonds in the LDH structure [51, 52].

Following post-treatment, the high resolution O 1s spectrum shows a slight shift to lower binding energy (531.81 to 530.96 eV) (**Table 4**). This may be related to the presence of additional Mn-O-Mn bonds (~530 eV) in the LDH structure [53]. This could also explain the increase in O content after Mn loading post-treatment (**Table 4**). This is in line with the Mn-O-Mn and Mn-O bond vibrations observed in FTIR (**Figure 6**).

The C 1s spectra in both Ca-Al-LDH and Ca-Al-LDH-Mn show the presence of CO₃²⁻ anions in the LDH structure [51] (**Figure S4**). The Ca 2p spectra confirm the presence of Ca-O bonds [52] (**Figure S5**). Ca-Al-LDH-Mn coating displayed lower C and Ca concentrations in comparison to Ca-Al-LDH coating (**Table 4**). The lower C content may be the result of an anion-exchange mechanism where CO₃²⁻ anions are replaced by MnO₄⁻. Additionally, the formation of Mn-rich deposits on the surface would also be responsible for the decreased signals of C and Ca in the layer thickness probed by XPS.

Mn manifests as a peak at the high-energy region of the spectrum (640-647 eV) in Ca-Al-LDH-Mn coating (**Figure 7b**). For detailed analysis, **Figure 8** shows the high-resolution XPS spectrum of Mn 2p. After peak fitting, the content of Mn in its different oxidation states was calculated (**Table 5**).

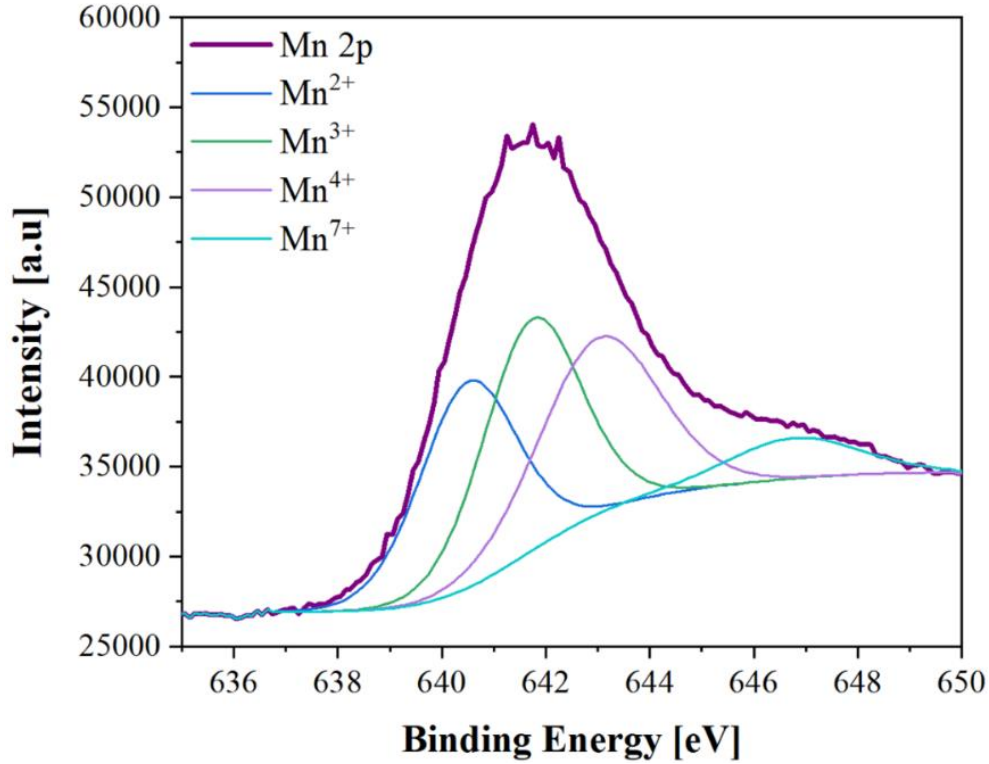


Figure 8. High-resolution XPS spectrum of Mn 2p for Ca-Al-LDH-Mn coating.

Table 5. XPS results for the Mn 2p level in the Ca-Al-LDH-Mn coating. Note that the total Mn content in the analysed surface amounts to 11.5 at. %.

Mn oxidation state	Binding energy (eV)	Peak area (%)	at. %
Mn ²⁺	640.5	29.1	3.3
Mn ³⁺	641.7	32.6	3.8
Mn ⁴⁺	643.0	30.6	3.5
Mn ⁷⁺	646.8	7.7	0.9

Table 5 shows similar concentrations of Mn²⁺, Mn³⁺ and Mn⁴⁺. The lower concentration of Mn⁷⁺ indicates that the Ca-Al-LDH-Mn coating contains a small amount of MnO₄⁻ anions in the LDH structure [30, 40]. This is attributed to the reduction of Mn(VII) during the Mn-loading process since in alkaline medium (pH 10) its reduction is highly favoured [32, 35, 36]. A similar result was observed by Yang *et al.* [40] for the incorporation of MnO₄⁻ in Mg-Al-LDH. They suggested that Mn²⁺ and Mn³⁺ isomorphically replaced Mg²⁺

and Al^{3+} in the LDH structure and, to some extent, reduced the intercalation of Mn^{7+} . They also suggested that Mn^{4+} existed as MnO_2 on the surface.

Therefore, it is possible that Mn^{2+} and Mn^{3+} also isomorphically substitute Ca^{2+} and Al^{3+} in the Ca-Al-LDH-Mn coating (the size of Ca^{2+} (1.10 Å) is similar to that of Mg^{2+} (0.8 Å) [41]). This premise is supported by the similar proportion of Mn in the present study and the study of Yang *et al.* The formation of brown/yellow MnO_2 was confirmed in the literature [54] and is in line with the characteristic colour change after Mn-based post-treatment observed in **Figure 2**.

3.2. Corrosion behaviour

Figure 9 depicts the Bode diagrams of Ca-Al-LDH and Ca-Al-LDH-Mn coatings after immersion in 3.5 wt. % NaCl for 1 hour and 28 days. **Figure S6** displays Bode diagrams ($|Z|$ vs f) at intermediate immersion times for Ca-Al-LDH and Ca-Al-LDH-Mn specimens.

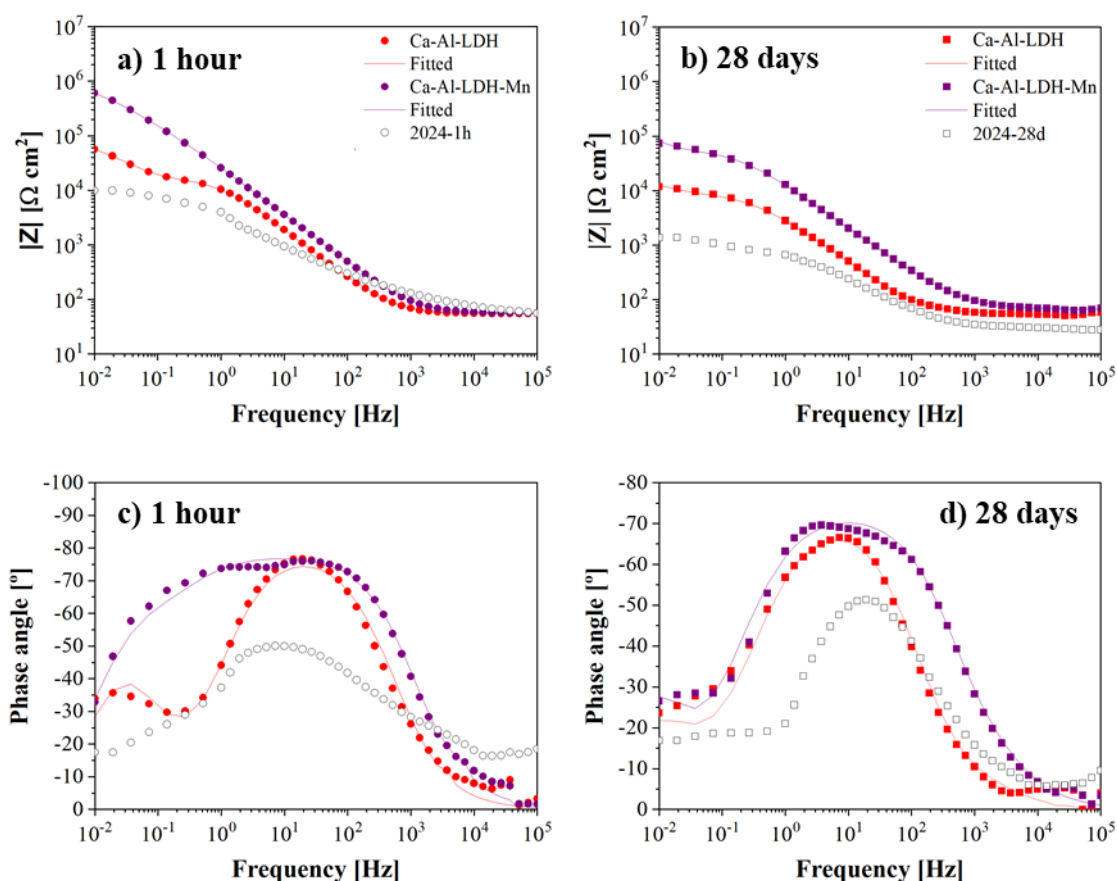


Figure 9. Bode plots of the Ca-Al-LDH and Ca-Al-LDH-Mn coatings after 1 hour and 28 days of immersion time in 3.5 wt. % NaCl solution.

The impedance modulus is a well-known indicator of the general corrosion resistance of LDH systems [55]. After 1 hour of immersion, the impedance modulus at 10^{-2} Hz of the Ca-Al-LDH-Mn coating ($5.8 \cdot 10^5 \Omega \text{ cm}^2$) is approximately one order of magnitude higher than that of the Ca-Al-LDH coating ($6.1 \cdot 10^4 \Omega \text{ cm}^2$) (**Figure 9a**). This demonstrates the positive effect of the Mn post-treatment.

Following 28 days of immersion, the observed drastic decrease of impedance at 10^{-2} Hz for Ca-Al-LDH ($1.2 \cdot 10^4 \Omega \text{ cm}^2$) and Ca-Al-LDH-Mn ($7.3 \cdot 10^4 \Omega \text{ cm}^2$) coatings indicates an acceleration of the kinetics of the overall corrosion process due to the penetration of Cl^- ions (**Figure 9b, d**) [16, 56]. In any case, the beneficial effect of Mn is still observed.

The electrochemical response in the Bode diagrams can be associated with three distinct parts of the coatings: (i) the flaky outer LDH layer at high frequencies (10^3 - 10^5 Hz); (ii) the denser inner LDH layer at medium frequencies (10^1 - 10^2 Hz), and (iii) the electrochemical activity at the substrate interface at low frequencies (10^0 - 10^{-2} Hz). It is worth noting that the time constants at high and medium frequencies show strong overlapping. The equivalent circuit with three-time constants shown in **Figure 10** was used to fit the experimental data. The calculated electrochemical parameters are presented in **Table 6**.

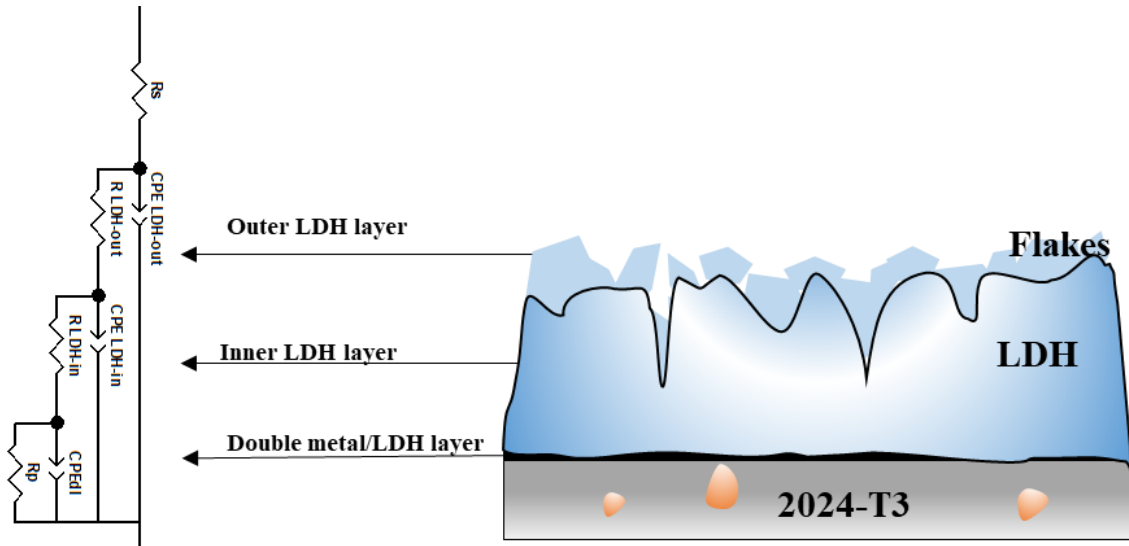


Figure 10. Equivalent circuit used to fit the EIS data of Ca-Al-LDH and Ca-Al-LDH-Mn coatings grown on AA2024-T3 substrate after 1 hour and 28 days of immersion in 3.5 wt. % NaCl solution.

R_s accounts for the resistance of the electrolyte. Constant phase elements (CPE) were used instead of capacitances to account for the non-ideal behaviour of the system. $\text{CPE}_{\text{LDH-out}}/\text{R}_{\text{LDH-out}}$ are ascribed to the capacitive and resistive behaviour of the outer LDH layer. $\text{CPE}_{\text{LDH-in}}/\text{R}_{\text{LDH-in}}$ are ascribed to the capacitive and resistive behaviour of the

inner LDH layer, and CPE_{dl}/R_p are ascribed to the double layer capacitance of the electrolyte/metal interface and the polarization resistance. This is in concordance with the bi-layer structure observed by TEM and the available literature [14, 57].

Table 6. Equivalent circuit data for Ca-Al-LDH and Ca-Al-LDH-Mn on 2024 alloy in 3.5 wt. % NaCl solution. The standard deviation values are shown in parentheses.

Coating	CPE LDH-out ($F s^{(n-1)} \cdot cm^{-2}$)	n LDH-out	R LDH-out (Ωcm^2)	CPE LDH-in ($F s^{(n-1)} \cdot cm^{-2}$)	n LDH-in	R LDH-in (Ωcm^2)	CPE_{dl} ($F s^{(n-1)} \cdot cm^{-2}$)	n_{dl}	R_p (Ωcm^2)
1 hour									
Ca-Al-LDH	$8.7 \cdot 10^{-6}$ ($\pm 1 \cdot 10^{-6}$)	0.82	21 (± 2)	$4.9 \cdot 10^{-6}$ ($\pm 1 \cdot 10^{-6}$)	0.91	$1.7 \cdot 10^4$ ($\pm 1 \cdot 10^3$)	$1.6 \cdot 10^{-4}$ ($\pm 2 \cdot 10^{-5}$)	0.93	$5.6 \cdot 10^4$ ($\pm 1 \cdot 10^3$)
Ca-Al-LDH-Mn	$9.5 \cdot 10^{-6}$ ($\pm 1 \cdot 10^{-7}$)	0.84	450 (± 40)	$1.1 \cdot 10^{-7}$ ($\pm 1 \cdot 10^{-9}$)	0.98	$2.9 \cdot 10^5$ ($\pm 1 \cdot 10^4$)	$5.7 \cdot 10^{-6}$ ($\pm 1 \cdot 10^{-6}$)	0.80	$5.2 \cdot 10^5$ ($\pm 1 \cdot 10^2$)
28 days									
Ca-Al-LDH	$9.7 \cdot 10^{-6}$ ($\pm 6 \cdot 10^{-7}$)	0.96	13 (± 4)	$6.1 \cdot 10^{-5}$ ($\pm 6 \cdot 10^{-6}$)	0.78	$9.1 \cdot 10^3$ ($\pm 4 \cdot 10^2$)	$1.4 \cdot 10^{-3}$ ($\pm 2 \cdot 10^{-4}$)	0.84	$1.1 \cdot 10^4$ ($\pm 2 \cdot 10^2$)
Ca-Al-LDH-Mn	$7.9 \cdot 10^{-6}$ ($\pm 5 \cdot 10^{-6}$)	0.85	80 (± 30)	$8.4 \cdot 10^{-6}$ ($\pm 5 \cdot 10^{-7}$)	0.77	$5.9 \cdot 10^4$ ($\pm 1 \cdot 10^3$)	$3.3 \cdot 10^{-4}$ ($\pm 1 \cdot 10^{-5}$)	0.77	$7.1 \cdot 10^4$ ($\pm 4 \cdot 10^3$)

After 1 hour of immersion, Ca-Al-LDH-Mn shows superior barrier properties ($R_{LDH-out}$, R_{LDH-in} , and R_p) than Ca-Al-LDH (**Table 6**). This enhanced corrosion resistance was equally confirmed by its lower CPE values [15, 18]. After 28 days of immersion, a decrease in the overall resistance and increase in CPE parameters is observed in both LDH coatings. This indicates that the electrolyte has penetrated through both Ca-Al-LDH and Ca-Al-LDH-Mn coatings and given rise to electrochemical activity at the substrate/coating interface [14, 56].

Considering the presence of Mn in the LDH structure evidenced by the SEM/EDS examinations (**Figure 3** and **Table 3**) and XPS analysis (**Figure 7**), the improved corrosion resistance of the Ca-Al-LDH-Mn coating may be attributed to the (i) hampered mass transport of aggressive species towards the electrolyte/metal interface due to the presence of Mn species in the coating and, (ii) hampered cathodic activity of the intermetallic compounds (IMCs) due to the formation of Mn-enriched deposits [31, 32].

Compared to other studies on the 2024 alloy coated with V-, Mo- and MBT-containing LDH coatings [14, 21, 22], the present Ca-Al-LDH-Mn coating provides a similar level of long-term barrier corrosion protection, while being considerably thinner and requiring a lesser preparation time.

In summary, EIS analysis confirmed enhanced barrier properties as a consequence of the Mn-loading step.

3.3. Water contact angle and paintability

The paintability is directly related to the material surface wettability and, therefore, contact angle measurements can be used as a useful predictive tool (i.e. low contact angle should correlate with high paintability). Both LDH coatings show high hydrophilicity with contact angle values of $(4\pm1)^\circ$ and $(26\pm6)^\circ$ for Ca-Al-LDH and Ca-Al-LDH-Mn, respectively. This is attributed to the porous structure of the LDH layers. Note that the differences in contact angle were different on a quantitative level but not on a qualitative level since both coatings are hydrophilic. To the authors' best knowledge, there are no studies available in the literature concerning the wettability of Mn-containing LDH or Mn-based conversion coatings. Therefore, the differences in wettability may be related to the homogeneous distribution of Mn species in the Ca-Al-LDH-Mn coating. This may hamper to some extent the penetration of water within the LDH structure.

Paint adhesion tests revealed an excellent performance (0 rating) for both coatings (**Figure 11**). Therefore, the presence of Mn-containing species in the LDH surface chemistry does not compromise paint adhesion.

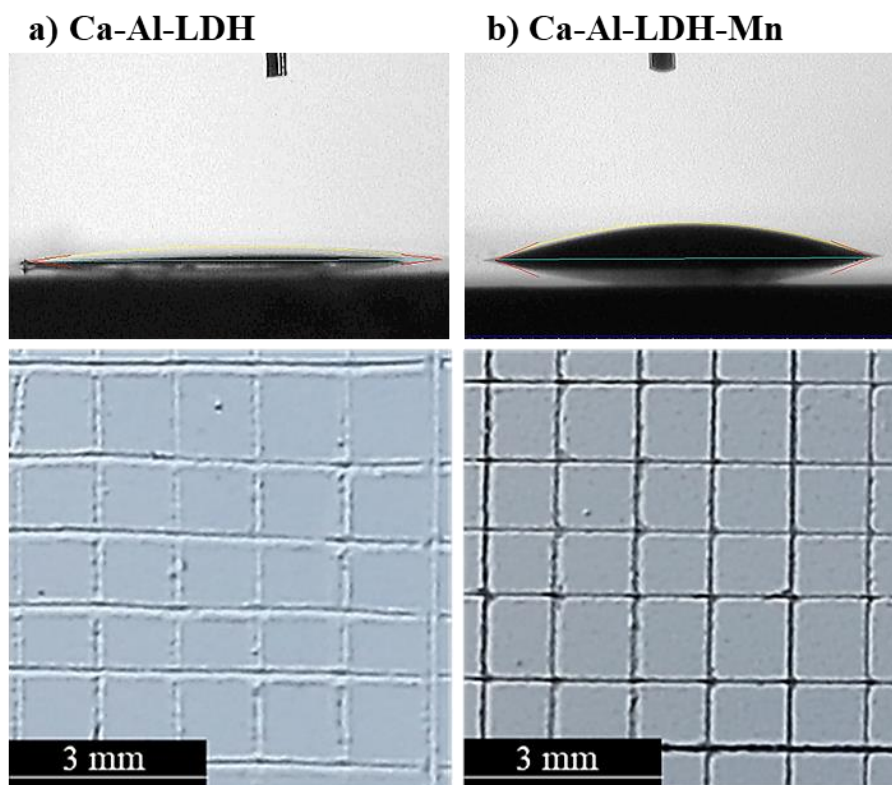


Figure 11. Water drop and surface appearance of painted LDH coatings surfaces after the paint adhesion test. Rating 0 for both Ca-Al-LDH and Ca-Al-LDH-Mn.

3.4. Evaluation of active corrosion protection

Figure 12 shows the surface appearance of scribed Ca-Al-LDH and Ca-Al-LDH-Mn specimens after immersion in 3.5 wt. % NaCl solution.

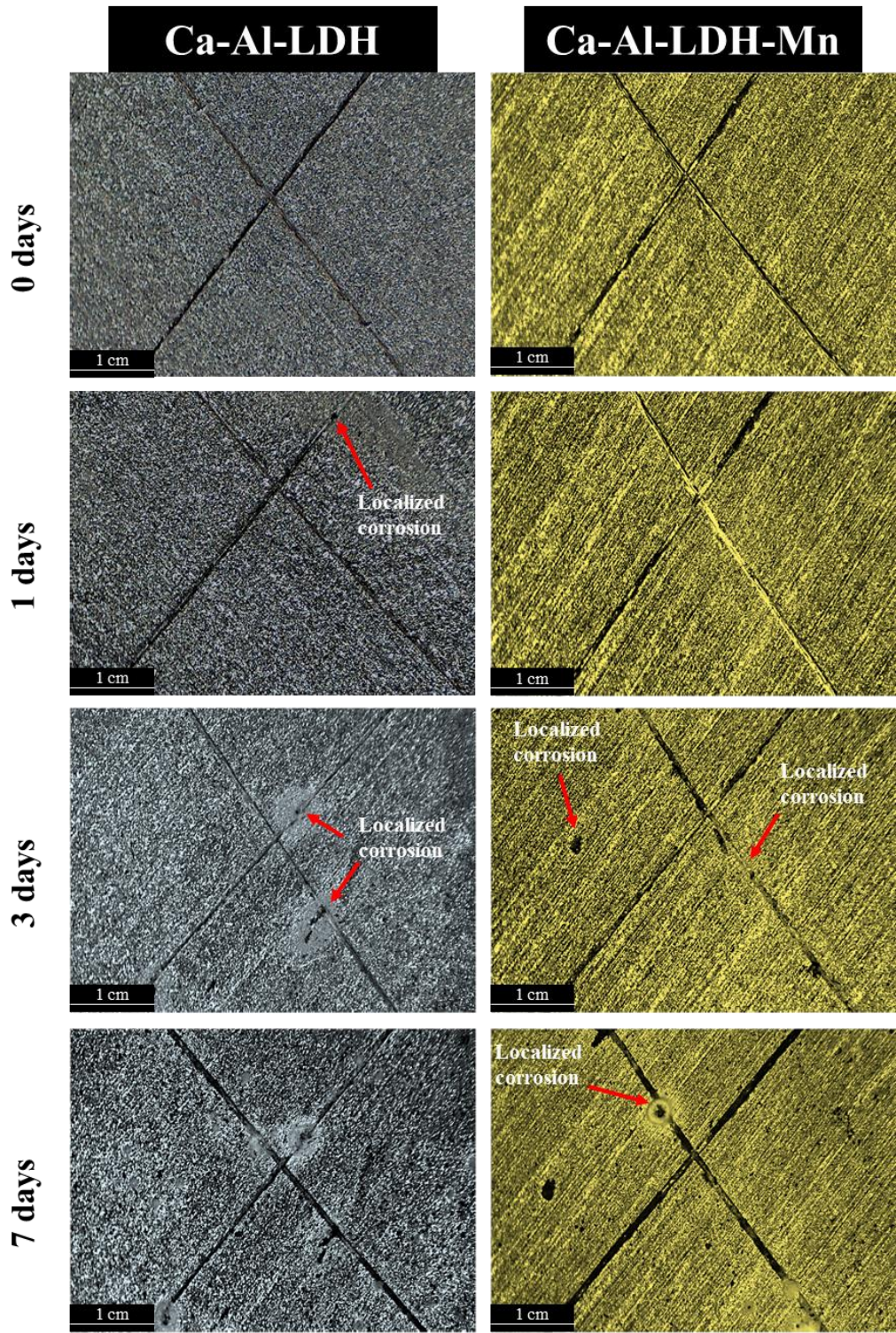


Figure 12. Surface appearance of Ca-Al-LDH and Ca-Al-LDH-Mn scribed coatings following immersion in 3.5 wt. % NaCl solution at different time points. Red arrows indicate the corrosion damage.

Localized corrosion for the Ca-Al-LDH specimen is observed just after one day of immersion. Then, the number and size of the damaged areas increase with the immersion time. Conversely, the Ca-Al-LDH-Mn coating provides longer-lasting protection (localized corrosion was only visible after 3 days). Note that the characteristic yellow/brown color of the Ca-Al-LDH-Mn specimen was preserved during the immersion test. This may be associated with the insoluble character of MnO_2 [32, 58] in the studied NaCl aqueous solution ($\text{pH } 6.6 \pm 0.2$).

Figure 13 shows the SEM micrographs of scribed LDH coatings before and after 7 days of immersion in 3.5 wt. % NaCl solution.

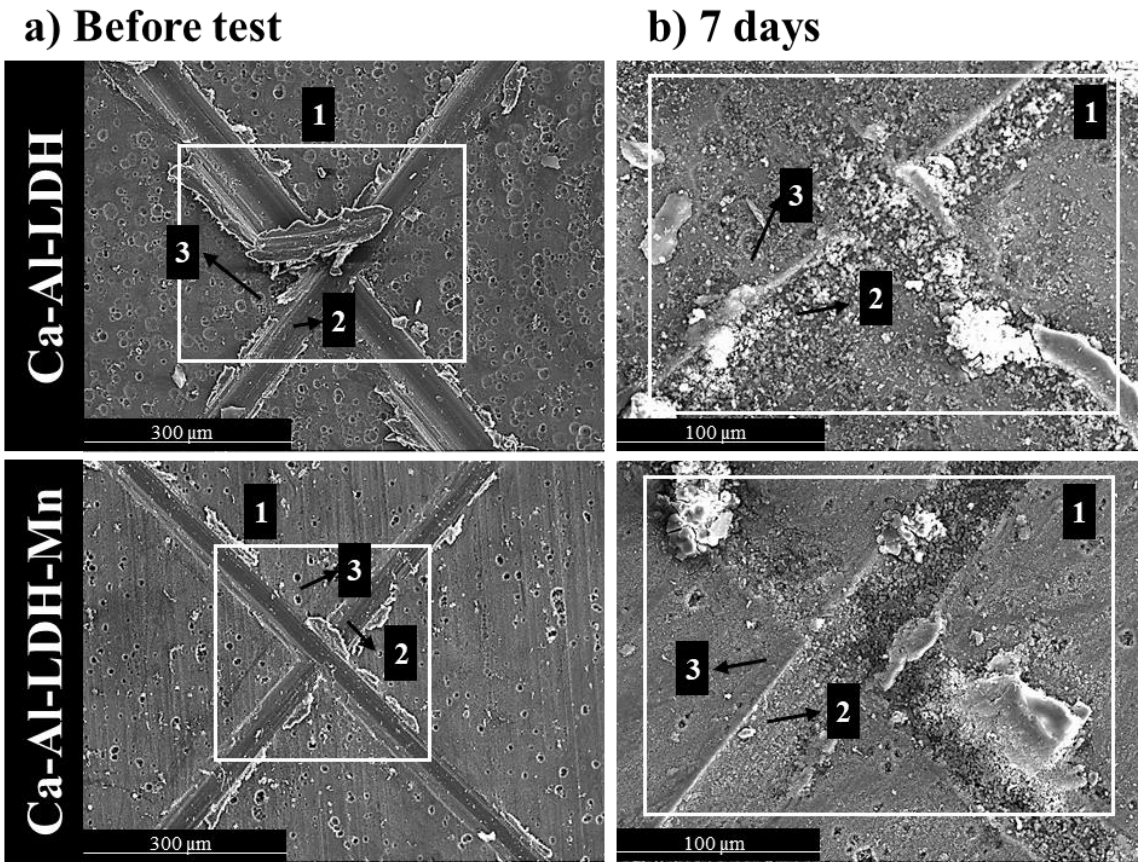


Figure 13. Scanning electron micrographs corresponding to the scribed plan views of Ca-Al-LDH and Ca-Al-LDH-Mn coatings (a) before the test and (b) after 7 days of immersion in 3.5 wt. % NaCl solution. Note that in each case EDS analyses have been performed of the general area comprising the scribe (1), inside the scribe (2), and of the coating outside the scribe (3).

EDS results in **Table 7** reveal that, in general, the concentration of Al decreased, while the O concentration increased after 7 days of immersion. This is related to the formation of Al (hydr)oxide compounds at the scribe and the coating surface. The presence of Cu

(from the IMCs) could be to some extent due to the voltage used for the EDS analysis and the low thickness of the Ca-Al-LDH and Ca-Al-LDH-Mn coatings.

In any case, the Ca-Al-LDH-Mn coating shows a lesser amount of corrosion products in comparison to the Mn-free coating. A more relevant result is that Mn is detected inside the scribe after 7 days of immersion (0.3 at. %, point 2 in Table 5), whereas Mn content notably decreases from 1.1 at. % to 0.2 at. % in the areas surrounding the scribe (Table 7, locations marked as 3 in Figure 13b).

Table 7. EDS (at. %) area analysis of scribed Ca-Al-LDH and Ca-Al-LDH-Mn coatings on 2024 alloy before and after 7 days of immersion in 3.5 wt. % NaCl solution.

Coating	Location		C	O	Mg	Al	Ca	Cu	Mn
Ca-Al-LDH	Before test	1	34.0	18.0	0.7	46.2	0.1	1.0	-
		2	36.7	4.0	0.9	57.4	-	1.0	-
		3	27.8	19.0	0.7	50.5	0.2	1.8	-
	After 7 days	1	22.5	46.1	0.4	30.2	-	0.8	-
		2	17.3	50.0	-	30.2	-	2.5	-
		3	19.6	47.0	0.3	32.2	-	0.9	-
Ca-Al-LDH-Mn	Before test	1	30.6	21.8	0.7	45.5	-	0.9	0.5
		2	28.3	4.7	1.1	64.6	-	1.3	-
		3	21.6	24.2	0.7	50.5	-	1.9	1.1
	After 7 days	1	22.9	45.3	0.4	30.4	-	0.8	0.2
		2	16.8	40.0	0.5	41.6	-	0.8	0.3
		3	19.0	25.5	0.8	53.5	-	1.0	0.2

The presence of Mn inside the scribe, where there was none before the immersion, indicates Mn release from the intact coating zones and subsequent precipitation. There are two possible sources for Mn; (i) partial dissolution of Mn-rich precipitates, such as the one located in point 2 of Figure 3b; and (ii) release of Mn^{2+} , Mn^{3+} and, to some extent, MnO_4^- ions from the LDH structure.

To the Authors' best knowledge, there are no studies in the literature concerning Mn-loaded LDH coatings for corrosion protection of Al alloys. However, some of the features found in this study are comparable to those reported for scratched Mn-loaded conversion coatings on 2024-T3 [30] and EV31 alloys [59] after neutral salt spray test (NSST). Namely, these studies also found Mn-containing products on the scribed surfaces.

Based on the results obtained in this study and the chemistry of Mn in the studied medium, the active corrosion protection mechanism in **Figure 14** is proposed for the Ca-Al-LDH-Mn system.

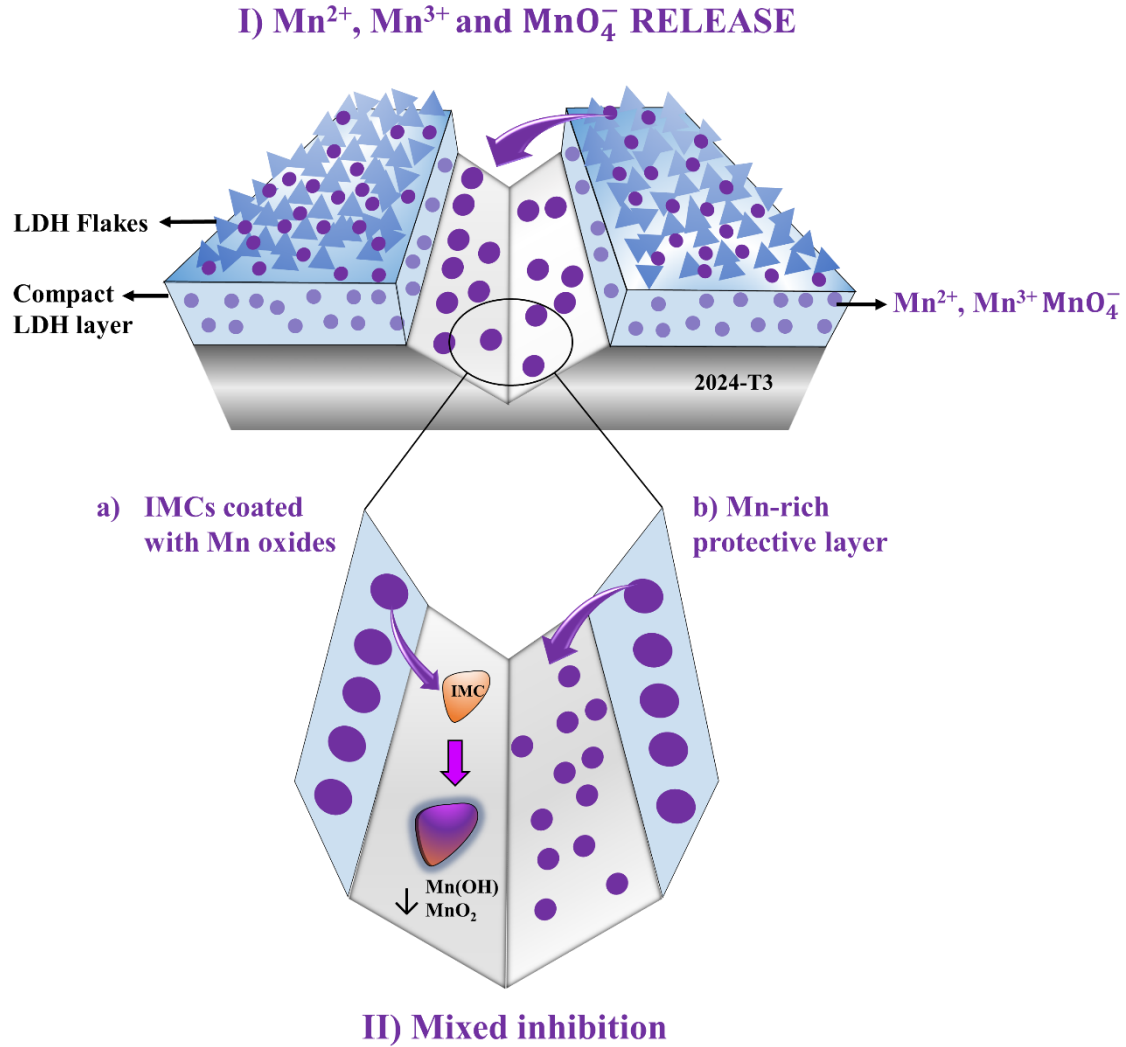
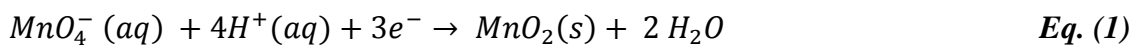


Figure 14. Schematic diagram of the active corrosion protection mechanism for the Ca-Al-LDH-Mn system (3.5 wt. % NaCl solution at pH 6.6 ± 0.2).

According to the Pourbaix diagram of Mn, MnO_4^- is a strong oxidizer due to its high equilibrium potential. Therefore, it is hypothesized that when liberated from the LDH interlayers, MnO_4^- ions will be spontaneously reduced when in contact with the bare Al substrate in the scribe according to the following reactions (**Equations 1 and 2**) [32]:

- Cathodic reaction:



- Anodic reaction: $Al \rightarrow Al^{3+} + 3e^-$ **Eq. (2)**

Additional electrochemical reactions can further reduce MnO_2 to Mn_2O_3 , Mn_3O_4 , MnO , Mn^{2+} and $\text{Mn}(\text{OH})_2$ [32, 60]. It is known that in permanganate solutions, Mn-rich products tend to precipitate over cathodic IMCs [3, 31, 32], mainly as MnO_2 and $\text{Mn}(\text{OH})_2$ [31, 32]. In other words, MnO_4^- typically acts as a cathodic inhibitor. In addition to the permanganate ions, the presence of Mn^{2+} could also contribute to the active protection mechanism. XPS results revealed that the coating surface contains Mn^{2+} . This could be in the form of deposits (e.g. MnO) or within the LDH structure replacing Ca^{2+} ions. Mn^{2+} liberated from deposits or the LDH structure would be converted to $\text{Mn}(\text{OH})_2$ by a chemical reaction at locations with alkaline pH (i.e. where the cathodic reaction takes place). Thus, both MnO_4^- and Mn^{2+} could be responsible for the active protection mechanism. Note that deposits that contain Mn^{3+} and Mn^{4+} species would be additional sources of Mn^{2+} upon reduction. In case of Mn^{3+} , its release from the LDH structure (where it replaces Al^{3+}) is also a possibility.

Figure 13b shows that rather than isolated Mn-rich deposits over IMCs, a relatively uniform layer enriched in Al, Mn and O is formed over the entire scribe. In a study with the alloy AA2024-T351 immersed in 0.05 M NaCl solution with relatively low KMnO_4 concentration (0.005 M) it was also found that Mn oxides covered both the intermetallic particles and the aluminium matrix [32]. As a result, an increased pitting potential was observed in that study. This ubiquity of Mn products over the IMCs and the aluminium matrix suggests that Mn-species act as mixed corrosion inhibitor under the studied conditions.

4. Conclusions

For the first time, *in situ* growth of a Ca-Al-LDH coating doped with MnO_4^- was successfully achieved on the 2024-T3 alloy. The main conclusions can be summarized as follows:

- The Ca-Al-LDH coating was successfully synthesized on the 2024-T3 alloy by *in situ* growth methodology.
- Ca-Al-LDH-Mn coating provided enhanced corrosion protection. Mn was detected in the LDH coating and as Mn-rich precipitates at the location of secondary phases. XPS results revealed that Mn was present mainly as Mn^{2+} , Mn^{3+} and Mn^{4+} . Traces of Mn^{7+} were also detected.

- Mn-loading decreased the hydrophilicity of the coating without compromising its excellent paintability.
- Corrosion testing of scribed specimens revealed that the incorporation of Mn into Ca-Al-LDH coating improved the coating stability and resulted in less degradation in comparison to Ca-Al-LDH coating.
- Active protection corrosion protection is demonstrated for the Ca-Al-LDH-Mn coating. The mechanism of inhibition involved the release of Mn species from the unscribed areas and the subsequent formation of Mn-rich (hydr)oxides at the coating scribe.

Taking into account the results presented in this study, Ca-Al-LDH-Mn could be used as a Cr-free conversion coating for painted components in the aircraft industry. However, further tests concerning active corrosion protection ability, up-scaling, and mechanical properties should be implemented in the future.

Acknowledgments/Funding

The authors gratefully acknowledge the support of the RTI2018-096391-B-C33 (MCIU/AEI/FEDER, UE), ADITIMAT-CM (S2018/NMT-4411, Regional Government of Madrid and EU Structural and Social Funds), and M. Mohedano is grateful for the support of RYC-2017 21843.

Data statement

The raw/process data required to reproduce these findings cannot be shared at this time as the data also forms part of an ongoing study.

Declaration of competing interest

The authors declare that they have no known competing financial interests or personal relationships that could have appeared to influence the work reported in this paper.

Credit authorship contribution statement

Ruben del Olmo: Conceptualization, Methodology, Investigation, Experimental part, Writing- Original draft preparation. **Marta Mohedano:** Experimental part, Review & Editing, Resources, and Project Administration. **Endzhe Matykina:** Experimental part, Supervision, Review & Editing, Resources, and Project Administration. **Raúl Arrabal**

560 **Durán:** Experimental part, Investigation, Supervision, Review & Editing, Resources, and
561 Project Administration.

562 **Bibliography:**

- 563 [1] C. Vargel, Chapter F.1 - Protection of aluminium, in: Corrosion of Aluminium
564 (Second Edition), C. Vargel (Ed.), Elsevier, Amsterdam, 2020, pp. 383-443.
- 565 [2] S. Cramer, ASM Handbook, Volume 13A - Corrosion: Fundamentals, Testing, and
566 Protection, ASM International, 2010-07-06.
- 567 [3] S. Kulinich, A. Akhtar, On Conversion Coating Treatments to Replace Chromating
568 for Al Alloys: Recent Developments and Possible Future Directions, Russian Journal of
569 Non-Ferrous Metals, 53 (2012) 176-203.
- 570 [4] LANXESS, Surface treatment for applications in the aeronautics and aerospace
571 industries., in, 2018, pp. 137.
- 572 [5] T.P. Schuman, Chapter 17 - Protective coatings for aluminum alloys, in: Handbook
573 of Environmental Degradation of Materials, M. Kutz (Ed.), William Andrew Publishing,
574 Norwich, NY, 2005, pp. 345-366.
- 575 [6] D.C. Beelen, P. Rouw, R. Boomgaard, K. Zabel, Aviox CF Primer: A new generation
576 primer for aircraft maintenance, Pigment & Resin Technology, 27 (1998) 28-33.
- 577 [7] A.E. Hughes, T.G. Harvey, N. Birbilis, A. Kumar, R.G. Buchheit, 7 - Coatings for
578 corrosion prevention based on rare earths, in: Rare Earth-Based Corrosion Inhibitors, M.
579 Forsyth, B. Hinton (Eds.), Woodhead Publishing, 2014, pp. 186-232.
- 580 [8] D. Mitton, A. Carangelo, A. Acquesta, T. Monetta, M. Curioni, F. Bellucci, Selected
581 Cr(VI) replacement options for aluminum alloys: A literature survey, Corrosion Reviews,
582 35 (2017).
- 583 [9] J. Qi, T. Hashimoto, J.R. Walton, X. Zhou, P. Skeldon, G. Thompson, Trivalent
584 chromium conversion coating formation on aluminium, Surface and Coatings
585 Technology, 280 (2015) 317-329.
- 586 [10] M.G.S. Ferreira, M.L. Zheludkevich, J. Tedim, Advanced protective coatings for
587 aeronautical applications, in: Nanocoatings and Ultra-Thin Films: Technologies and
588 Applications, 2011, pp. 235-279.
- 589 [11] X. Guo, F. Zhang, D. Evans, X. Duan, Layered double hydroxide films: Synthesis,
590 properties and applications, Chemical communications (Cambridge, England), 46 (2010)
591 5197-5210.
- 592 [12] K.A. Yasakau, M.L. Zheludkevich, M.G.S. Ferreira, Corrosion and Corrosion
593 Protection of Aluminum Alloys, in: Encyclopedia of Interfacial Chemistry, K. Wandelt
594 (Ed.), Elsevier, Oxford, 2018, pp. 115-127.
- 595 [13] D.G. Evans, R.C.T. Slade, Structural Aspects of Layered Double Hydroxides, in:
596 Layered Double Hydroxides, X. Duan, D.G. Evans (Eds.), Springer Berlin Heidelberg,
597 Berlin, Heidelberg, 2006, pp. 1-87.
- 598 [14] J. Tedim, M.L. Zheludkevich, A.C. Bastos, A.N. Salak, A.D. Lisenkov, M.G.S.
599 Ferreira, Influence of preparation conditions of Layered Double Hydroxide conversion
600 films on corrosion protection, Electrochimica Acta, 117 (2014) 164-171.
- 601 [15] J. Tedim, A.I. Kuznetsova, A. Salak, M. Montemor, D. Snihirova, M. Pilz, M.L.
602 Zheludkevich, M. Ferreira, Zn-Al layered double hydroxides as chloride nanotraps in
603 active protective coatings, Corrosion Science, 55 (2012) 1-4.
- 604 [16] M.L. Zheludkevich, S.K. Poznyak, L.M. Rodrigues, D. Raps, T. Hack, L.F. Dick, T.
605 Nunes, M.G.S. Ferreira, Active protection coatings with layered double hydroxide
606 nanocontainers of corrosion inhibitor, Corrosion Science, 52 (2010) 602-611.

- [17] A.C. Bouali, M. Serdechnova, C. Blawert, J. Tedim, M.G.S. Ferreira, M.L. Zheludkevich, Layered double hydroxides (LDHs) as functional materials for the corrosion protection of aluminum alloys: A review, *Applied Materials Today*, 21 (2020) 100857.
- [18] J. Tedim, M.L. Zheludkevich, A. Salak, A.D. Lisenkov, M. Ferreira, Nanostructured LDH-container layer with active protection functionality, *Journal of Materials Chemistry*, 21 (2011) 15464-15470.
- [19] J. Wu, D. Peng, Y. He, X. Du, Z. Zhang, B. Zhang, X. Li, Y. Huang, In Situ Formation of Decavanadate-Intercalated Layered Double Hydroxide Films on AA2024 and their Anti-Corrosive Properties when Combined with Hybrid Sol Gel Films, *Materials (Basel)*, 10 (2017) 426.
- [20] J. Tedim, M.L. Zheludkevich, A.C. Bastos, A.N. Salak, J. Carneiro, F. Maia, A.D. Lisenkov, A.B. Oliveira, M.G.S. Ferreira, Effect of surface treatment on the performance of LDH conversion films, *ECS Electrochemistry Letters*, 3 (2014) C4-C8.
- [21] Y. Zhang, J. Liu, I. Yingdong, M. Yu, S. Li, B. Xue, Fabrication of inhibitor anion-intercalated layered double hydroxide host films on aluminum alloy 2024 and their anticorrosion properties, *Journal of Coatings Technology and Research*, 12 (2015) 293–302.
- [22] Y. Zhang, Y. Li, Y. Ren, H. Wang, F. Chen, Double-doped LDH films on aluminum alloys for active protection, *Materials Letters*, 192 (2017) 33-35.
- [23] Y. Zhang, P. Yu, J. Wang, Y. Li, F. Chen, K. Wei, Y. Zuo, LDHs/graphene film on aluminum alloys for active protection, *Applied Surface Science*, 433 (2018) 927-933.
- [24] S.U. Ofoegbu, F.A.O. Fernandes, A.B. Pereira, The Sealing Step in Aluminum Anodizing: A Focus on Sustainable Strategies for Enhancing Both Energy Efficiency and Corrosion Resistance, *Coatings*, 10 (2020) 226.
- [25] F. Millange, R. Walton, L. Lei, D. O'Hare, Efficient Separation of Terephthalate and Phthalate Anions by Selective Ion-Exchange Intercalation in the Layered Double Hydroxide $\text{Ca}_2\text{Al}(\text{OH})_6 \cdot \text{NO}_3 \cdot 2\text{H}_2\text{O}$, *Chemistry of Materials - CHEM MATER*, 12 (2000) 1990-1994.
- [26] M. Meyn, K. Beneke, G. Lagaly, Anion-exchange reactions of layered double hydroxides, *Inorganic Chemistry*, 29 (1990) 5201-5207.
- [27] A.V. Radha, P. Vishnu Kamath, C. Shivakumara, Mechanism of the anion exchange reactions of the layered double hydroxides (LDHs) of Ca and Mg with Al, *Solid State Sciences*, 7 (2005) 1180-1187.
- [28] M. Iqbal, L. Sun, A. LaChance, H. Ding, M. Fedel, In situ Growth of CaAl-NO_3 --Layered Double Hydroxide Directly on Aluminum Alloy for Corrosion Resistance, *Dalton Transactions*, 49 (2019).
- [29] A. Pardo, S. Feliu, M. Merino, R. Arrabal, E. Matykina, XPS Study of Chemical Changes on the La/Ce Treated Surface of A361 Aluminium Alloy Exposed to Air at Temperatures up to 500°C, *Advances in Materials Science and Engineering*, (2009).
- [30] G. Yoganandan, J.N. Balaraju, V.K. William Grips, The surface and electrochemical analysis of permanganate based conversion coating on alclad and unclad 2024 alloy, *Applied Surface Science*, 258 (2012) 8880-8888.
- [31] S.A. Kulinich, M. Farzaneh, X.W. Du, Growth of corrosion-resistant manganese oxide coatings on an aluminum alloy, *Inorganic Materials*, 43 (2007) 956-963.
- [32] S.B. Madden, J.R. Scully, Inhibition of AA2024-T351 Corrosion Using Permanganate, *Journal of The Electrochemical Society*, 161 (2014) C162-C175.
- [33] B. Dou, Y. Wang, T. Zhang, B. Liu, Y. Shao, G. Meng, F. Wang, Growth behaviors of layered double hydroxide on microarc oxidation film and anti-corrosion performances of the composite film, *Journal of the Electrochemical Society*, 163 (2016) C917-C927.

- [34] F. Zhang, C.L. Zhang, L. Song, R.C. Zeng, Z.G. Liu, H.Z. Cui, Corrosion of in-situ grown MgAl-LDH coating on aluminum alloy, *Transactions of Nonferrous Metals Society of China (English Edition)*, 25 (2015) 3498-3504.
- [35] K.M. Dietmann, T. Linke, M.D. Nogal Sánchez, J.L. Pérez Pavón, V. Rives, Layered Double Hydroxides with Intercalated Permanganate and Peroxydisulphate Anions for Oxidative Removal of Chlorinated Organic Solvents Contaminated Water, *Minerals*, 10 (2020).
- [36] J.D. Hem, Chemical equilibria and rates of manganese oxidation, in: geological survey water-supply paper 1667-A, united states government printing office, washington, 1963.
- [37] M. Szabados, R. Mészáros, S. Erdei, Z. Kónya, Á. Kukovecz, P. Sipos, I. Pálínkó, Ultrasonically-enhanced mechanochemical synthesis of CaAl-layered double hydroxides intercalated by a variety of inorganic anions, *Ultrasonics Sonochemistry*, 31 (2016) 409-416.
- [38] E. Herald, K.D. Nugrahaningtyas, Heriyanto, X-ray Diffraction Analysis on Post Treatment of Ca-Mg-Al-Layered Double Hydroxide Slurry, *IOP Conference Series: Materials Science and Engineering*, 176 (2017) 012020.
- [39] G. Varga, Á. Kukovecz, Z. Kónya, L. Korecz, S. Muráth, Z. Csendes, G. Peintler, S. Carlson, P. Sipos, I. Pálínkó, Mn(II)-amino acid complexes intercalated in CaAl-layered double hydroxide - Well-characterized, highly efficient, recyclable oxidation catalysts, *Journal of Catalysis*, 335 (2016) 125-134.
- [40] C. Yang, L. Liao, G. Lv, L. Wu, L. Mei, Z. Li, Synthesis and characterization of Mn intercalated Mg-Al hydrotalcite, *Journal of Colloid and Interface Science*, 479 (2016) 115-120.
- [41] J.L. Milagres, C.R. Bellato, R.S. Vieira, S.O. Ferreira, C. Reis, Preparation and evaluation of the Ca-Al layered double hydroxide for removal of copper(II), nickel(II), zinc(II), chromium(VI) and phosphate from aqueous solutions, *Journal of Environmental Chemical Engineering*, 5 (2017) 5469-5480.
- [42] A. Korchef, M. Touaibi, Effect of pH and temperature on calcium carbonate precipitation by CO₂ removal from iron-rich water, *Water and Environment*, 34 (2020) 331-341.
- [43] M.A. Iqbal, M. Secchi, M.A. Iqbal, M. Montagna, C. Zanella, M. Fedel, MgAl-LDH/graphene protective film: Insight into LDH-graphene interaction, *Surface and Coatings Technology*, 401 (2020) 126253.
- [44] A.C. Bouali, M.H. Iuzviuk, M. Serdechnova, K.A. Yasakau, D. Drozdenko, A. Lutz, K. Fekete, G. Dovzhenko, D.C.F. Wieland, H. Terryn, M.G.S. Ferreira, I.A. Zobkalo, M.L. Zheludkevich, Mechanism of LDH Direct Growth on Aluminum Alloy Surface: A Kinetic and Morphological Approach, *The Journal of Physical Chemistry C*, 125 (2021) 11687-11701.
- [45] M. Shabanian, M. Hajibeygi, A. Raeisi, 2 - FTIR characterization of layered double hydroxides and modified layered double hydroxides, in: *Layered Double Hydroxide Polymer Nanocomposites*, S. Thomas, S. Daniel (Eds.), Woodhead Publishing, New York, 2020, pp. 77-101.
- [46] S. Aisawa, H. Hirahara, H. Uchiyama, S. Takahashi, E. Narita, Synthesis and Thermal Decomposition of Mn-Al Layered Double Hydroxides, *Journal of Solid State Chemistry*, 167 (2002) 152-159.
- [47] J.T. Klopogge, R.L. Frost, Fourier Transform Infrared and Raman Spectroscopic Study of the Local Structure of Mg-, Ni-, and Co-Hydrotalcites, *Journal of Solid State Chemistry*, 146 (1999) 506-515.

- [48] H. Chen, J. He, Facile Synthesis of Monodisperse Manganese Oxide Nanostructures and Their Application in Water Treatment, *The Journal of Physical Chemistry C*, 112 (2008) 17540-17545.
- [49] M. Zheng, H. Zhang, X. Gong, R. Xu, Y. Xiao, H. Dong, X. Liu, Y. Liu, A simple additive-free approach for the synthesis of uniform manganese monoxide nanorods with large specific surface area, *Nanoscale research letters*, 8 (2013) 166.
- [50] Y. Wang, Y. Zhang, B. Zhou, C. Li, F. Gao, X. Wang, D. Liang, Y. Wei, In-situ observation of the growth behavior of ZnAl layered double hydroxide film using EQCM, *Materials & Design*, 180 (2019) 107952.
- [51] J. Zhu, Z. Zhu, H. Zhang, H. Lu, Y. Qiu, Efficient degradation of organic pollutants by peroxymonosulfate activated with MgCuFe-layered double hydroxide, *RSC Advances*, 9 (2019) 2284-2291.
- [52] Y. Zou, X. Wang, F. Wu, S. Yu, Y. Hu, W. Song, Y. Liu, H. Wang, T. Hayat, X. Wang, Controllable Synthesis of Ca-Mg-Al Layered Double Hydroxides and Calcined Layered Double Oxides for the Efficient Removal of U(VI) from Wastewater Solutions, *ACS Sustainable Chemistry & Engineering*, 5 (2017) 1173-1185.
- [53] L. He-Ming, Y.-X. Sun, F. Zhang, D.-Y. Zhang, Y.-F. Zhang, Preparation and electrochemical applications of spherical maltose-based templated carbon/MnOx composite materials, *Electrochimica Acta*, 148 (2014).
- [54] Z. Khan, S. Ahmed Al- Thabaiti, A. Yousif Obaid, Z.A. Khan, MnO₂ nanostructures of different morphologies from amino acids-MnO₄⁻ reactions in aqueous solutions, *Colloids and Surfaces B: Biointerfaces*, 81 (2010) 381-384.
- [55] M.A. Iqbal, L. Sun, A.T. Barrett, M. Fedel, Layered Double Hydroxide Protective Films Developed on Aluminum and Aluminum Alloys: Synthetic Methods and Anti-Corrosion Mechanisms, 10 (2020) 428.
- [56] J. Wu, D. Peng, Y. He, X. Du, Z. Zhang, B. Zhang, X. Li, Y. Huang, In situ formation of decavanadate-intercalated layered double hydroxide films on AA2024 and their anti-corrosive properties when combined with hybrid sol gel films, *Materials*, 10 (2017).
- [57] J. Tedim, A.C. Bastos, S. Kallip, M.L. Zheludkevich, M.G.S. Ferreira, Corrosion protection of AA2024-T3 by LDH conversion films. Analysis of SVET results, *Electrochimica Acta*, 210 (2016) 215-224.
- [58] H.A. Swain, C. Lee, R.B. Rozelle, Determination of the solubility of manganese hydroxide and manganese dioxide at 25.deg. by atomic absorption spectrometry, *Analytical Chemistry*, 47 (1975) 1135-1137.
- [59] S.-Y. Jian, C.-Y. Yang, J.-K. Chang, Robust corrosion resistance and self-healing characteristics of a novel Ce / Mn conversion coatings on EV31 magnesium alloys, *Applied Surface Science*, 510 (2020) 145385.
- [60] N. Takeno, Atlas of Eh-pH diagrams - Intercomparison of thermodynamic databases, in: GSJ (Ed.) Geological Survey of Japan, AIS, 2005.